The Meteoritical Society

Meteoritics & Planetary Science 43, Nr 1/2, 41–73 (2008)
Abstract available online at http://meteoritics.org

Dust from comet Wild 2: Interpreting particle size, shape, structure, and composition from impact features on the Stardust aluminum foils

A. T. KEARSLEY[1*], J. BORG[2], G. A. GRAHAM[3], M. J. BURCHELL[4], M. J. COLE[4], H. LEROUX[5], J. C. BRIDGES[6], F. HÖRZ[7], P. J. WOZNIAKIEWICZ[1, 8], P. A. BLAND[8], J. P. BRADLEY[3], Z. R. DAI[3], N. TESLICH[3], T. SEE[9], P. HOPPE[10], P. R. HECK[10], J. HUTH[10], F. J. STADERMANN[11], C. FLOSS[11], K. MARHAS[11], T. STEPHAN[12], and J. LEITNER[12]

[1]Impacts and Astromaterials Research Centre, Department of Mineralogy, Natural History Museum, London SW7 5BD, UK
[2]Institut d'Astrophysique Spatiale (IAS), CNRS, Univ. Paris-Sud-UMR8617, Orsay Cedex F-91405, France
[3]Institute of Geophysics and Planetary Physics, Lawrence Livermore National Laboratory, Livermore, California, USA
[4]Centre for Astrophysics and Planetary Sciences, University of Kent, Canterbury, Kent CT2 7NH, UK
[5]Laboratoire de Structure et Propriétés de l'Etat Solide, Université de Lille, F-59655 Villeneuve d'Ascq, France
[6]Space Research Centre, Department of Physics and Astronomy, University of Leicester, University Road, Leicester LE1 7RH, UK
[7]ARES, NASA Johnson Space Center, Houston, Texas 77058, USA
[8]Impacts and Astromaterials Research Centre, Department of Earth Sciences and Engineering, Imperial College of Science Technology and Medicine, Prince Consort Road, London SW7 2AZ, UK
[9]Engineering and Science Contract Group, NASA Johnson Space Craft Center, Houston, Texas 77058, USA
[10]Max Planck Institute for Chemistry, Particle Chemistry Department, P.O. Box 3060, 55020 Mainz, Germany
[11]Department of Physics, Washington University, Saint Louis, Missouri 63130, USA
[12]Institut für Planetologie, Westfälische Wilhelms-Universität Münster, Wilhelm-Klemm-Str.10, 48149 Münster, Germany
[*]Corresponding author. E-mail: antk@nhm.ac.uk

(Submitted 11 April 2007; revision accepted 14 August 2007)

Abstract–Aluminum foils of the Stardust cometary dust collector are peppered with impact features of a wide range of sizes and shapes. By comparison to laboratory shots of known particle dimensions and density, using the same velocity and incidence geometry as the Stardust Wild 2 encounter, we can derive size and mass of the cometary dust grains. Using scanning electron microscopy (SEM) of foil samples (both flown on the mission and impacted in the laboratory) we have recognized a range of impact feature shapes from which we interpret particle density and internal structure. We have documented composition of crater residues, including stoichiometric material in 3 of 7 larger craters, by energy dispersive X-ray microanalysis. Wild 2 dust grains include coarse (>10 μm) mafic silicate grains, some dominated by a single mineral species of density around 3–4 g cm^{-3} (such as olivine). Other grains were porous, low-density aggregates from a few nanometers to 100 μm, with an overall density that may be lower than 1 g cm^{-3}, containing mixtures of silicates and sulfides and possibly both alkali-rich and mafic glass. The mineral assemblage is very similar to the most common species reported from aerogel tracks. In one large aggregate crater, the combined diverse residue composition is similar to CI chondrites. The foils are a unique collecting substrate, revealing that the most abundant Wild 2 dust grains were of sub-micrometer size and of complex internal structure. Impact residues in Stardust foil craters will be a valuable resource for future analyses of cometary dust.

INTRODUCTION

Abundant impact features of a wide range of shape and size have been reported on the Stardust aluminum (Al) foils in the Preliminary Examination (PE) summary by Hörz et al. (2006), including implications for the dust flux in the passage of Stardust through the comet Wild 2 coma. In this paper we present many additional observations of Al foil cometary dust craters seen during PE, and in particular explore the range of crater sizes, shapes, and residue compositions, with detailed examples from which we can interpret impacting particle size, mass, composition, and internal structure. As the Stardust encounter conditions (with the possible exception of secondary impacts discussed by Westphal et al. 2008) are well understood and can be replicated in laboratory experiments (e.g., Kearsley et al.

2006, 2007), we are confident that we can make extensive interpretation of Wild 2 dust characteristics from impacts on the Al foils.

Why use impact craters to study the structure, grain size, and composition of cometary dust? The very characteristics of silica aerogel that make it an effective capture medium, allowing deep embedding of grains that may have suffered only low shock pressures also compromise the interpretation of particle structure. There is abundant evidence from the Stardust PE that fragile grain aggregates have disintegrated during impact on the aerogel (Flynn et al. 2006; Hörz et al. 2006; Zolensky et al. 2006), rendering the characterization of most particle bulk properties difficult and/or impractical. Furthermore, the sub-micrometer size fraction cannot be easily identified in the aerogel, yet generates the most numerous impact craters in the Al foil. Despite the higher shock pressures (Stöffler 1982) and associated partial melting suffered by particles impacting onto Al foil, the lack of particle dispersion permits a more accurate measurement of particle size, density, mass, and porosity when compared to aerogel capture. Small particle impacts on metal substrates have also been extensively studied in the laboratory (Hörz et al. 1983; Bernhard and Hörz 1995; Burchell and MacKay 1998; Kearsley et al. 2006, 2007) and on space-exposed surfaces (e.g., Bernhard et al. 1994a, 1994b; Brownlee et al. 1994; Love et al. 1995; Graham et al. 2001). For known conditions of velocity and incidence angle, which are both well constrained for the Stardust Wild 2 encounter (Brownlee et al. 2003; Tsou et al. 2003), there is a relatively simple relationship between particle size and crater diameter (Kearsley et al. 2006), although it is also important to apply an appropriate particle density calibration (Kearsley et al. 2007). Particle density can be estimated by measuring the impact feature depth profile from stereometric analysis of tilted crater images (Kearsley et al. 2007). The same three-dimensional shape analysis can reveal whether an impact feature was created by a single, equant particle (creating a simple bowl shape), or by a porous aggregate of smaller particles (creating a broad, irregular compound feature comprising overlapping bowls). The presence of both these morphologies in Stardust foil craters of all sizes was shown by Hörz et al. (2006). The preservation of analyzable projectile residue has been demonstrated on a variety of space-exposed surfaces (e.g., Levine 1993; Graham et al. 2001; Kearsley et al. 2005) and in laboratory craters made by impact of mafic silicate projectiles (Kearsley et al. 2007). The potential for determination of the particle composition and even mineralogy from Stardust craters is seen in the data of Flynn et al. (2006) and Zolensky et al. (2006). The relatively low silicon content of the Al foil itself (~300 ppm; Kearsley et al. 2007) permits determination of silicon in the silicate particle residues without interference from the ubiquitous silica that encases and invades particles captured in aerogel. However, ever-present Al does prevent in situ determination of this important element in most crater residues, unless ultrathin sections are prepared from residue samples that may be free from the metal substrate (e.g., Leroux et al. 2008).

In this paper, we give an extensive account of the range of crater size and shape, the analysis of preserved dust residues, and the implications for understanding the size, structure, and composition of comet Wild 2 dust, in examples drawn from a sample of almost 300 Stardust foil impacts, with particular emphasis on seven large craters with diameters greater than 50 μm created by particles of greater than nanogram mass. For the smallest dust size fraction, that responsible for ~95% of all the craters found, we give a statistical analysis of the distribution of composition with crater size. In discussing specific examples, we use the foil nomenclature of the Stardust sample repository at NASA JSC, Houston, as shown at http://curator.jsc.nasa.gov/stardust/sample_catalog/SampleNomenclature.pdf.

MATERIALS STUDIED

The Al1100 series alloy (specifically, Al1145, temper 0) foil sheets, wrapped around the Stardust collector frame (Fig. 1) were used to hold the aerogel blocks gently in place during assembly, flight, and recovery. Prior to harvesting of aerogel blocks and their surrounding foils, a systematic, collector-wide survey of all craters >20 μm in diameter was conducted using a custom-made, large-scale x/y scanning platform and a Leica MZ16 stereomicroscope, as illustrated in Fig. 2a. Magnification was 80×, sufficient to recognize features 10 μm in size, yet the foil surfaces were of highly variable quality, in part rough, commonly covered with aerogel debris and frequently scratched, some badly. As a consequence, reliable identification of craters was possible only for features >20 μm in diameter. This survey yielded a total of 63 craters >20 μm on 123 cm^2 of foil (their distribution on the tray is illustrated in Fig. 4). The largest crater measured 480 μm across, sufficiently large to penetrate the 100 μm thick foil and to terminate in the underlying Al-frame. There is a non-random distribution of smaller impact locations, with statistically significant spatial clusters discussed in depth by Westphal et al. (2008).

On de-integration of the collector components, the narrow top foil surface was cut along its edges using the twin rotary cutter (Fig. 2b), releasing the unexposed Al foil tabs beside the aerogel block, and allowing the block to be carefully withdrawn. This foil cutting resulted in thin Al strips (long strips about 34 mm in length and 1.7 mm in width, and short strips of 13 mm by 1.7 mm) that were carefully stored and shipped to PE participants in small diameter (6 mm) glass vials to avoid any surface contact and potential post-flight contamination.

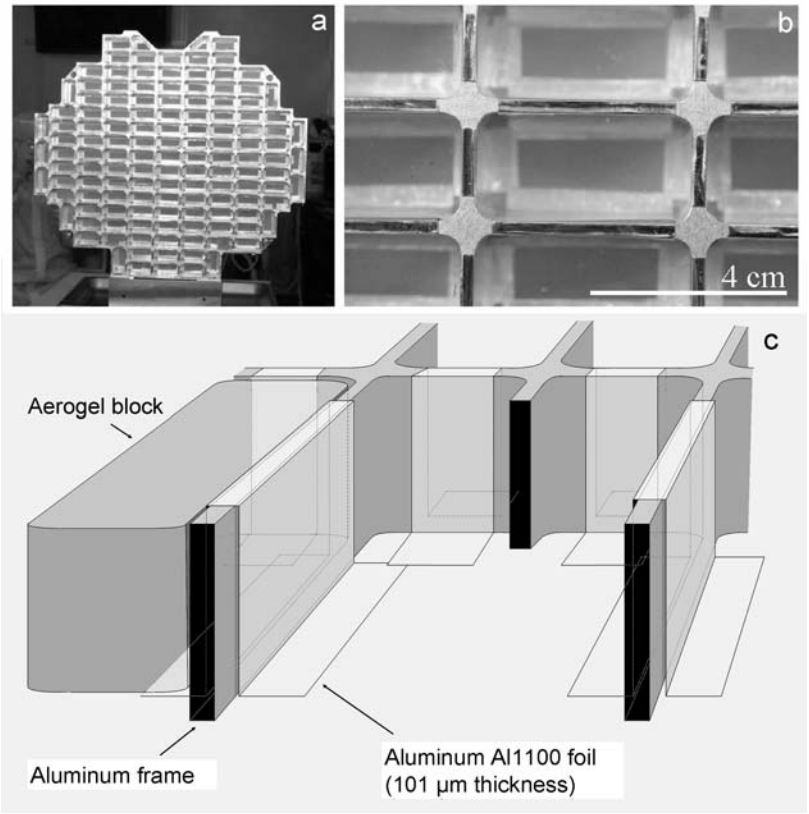

Fig. 1. a) The Stardust cometary dust collector with a rigid Al frame containing silica aerogel blocks and Al foil tabs. b) The location of Al foils around a single aerogel block. c) Schematic diagram showing the arrangement of Al1145 foil sheets wrapped around the Al frame and folded over the rear of aerogel blocks.

Locating and Imaging Foil Craters in the Scanning Electron Microscope

When prepared for scanning electron microscopy (SEM), to prevent contamination of the foil surface, to avoid close contact with adhesives, and minimize physical damage to the foil surface, the foils were not permanently attached to a mount, but were held flat and restrained from movement by a variety of methods, e.g., straps of high-purity tin wire or Al plate. A wide range of SEM instruments were used in the different institutions involved in the survey phase of the Stardust cratering preliminary evaluation, where the primary purpose was to determine the number and size range of impact features on numerous foil samples, as described in Hörz et al. (2006). For relatively low-magnification imagery and analysis (e.g., <1000× magnification work on larger craters at NHM) conventional tungsten filament electron gun instruments proved satisfactory, operating at 20 kV accelerating voltage and beam current of 2 nA. For smaller craters, low accelerating voltage field-emission SEM was used, giving high-quality images of impact features as small as 102 nm in diameter, with detail down to a few tens of nm in scale. Both secondary electron images (SEI) and backscattered electron images (BEI) proved useful, the former at all magnifications, the latter particularly for craters >20 μm in diameter. Representative crater images obtained during the Stardust PE are posted on http://curator.jsc.nasa.gov/stardust. Stereo imagery for three-dimensional crater shape reconstruction and production of digital elevation models (DEM) was performed using the protocol described in Kearsley et al. (2007).

IMPACTING PARTICLE SIZE AND MASS

In this paper, we employ the relationship between particle size and crater top-lip diameter established by Kearsley et al. (2006), based on light-gas gun shots of soda-lime glass spheres with a density of about 2.4 g cm^{-3}, fired perpendicular to Stardust Al1145 foil at a velocity close to 6.1 km s^{-1} (the Stardust Wild 2 encounter velocity), using the technique of Burchell et al. (1999). Six projectile sizes between 9.5 and 84 μm in diameter were used, yielding suites of circular craters (<10% variation in diameter) of between approximately 30 μm and 350 μm top lip diameter, therefore bracketing the size range of the larger

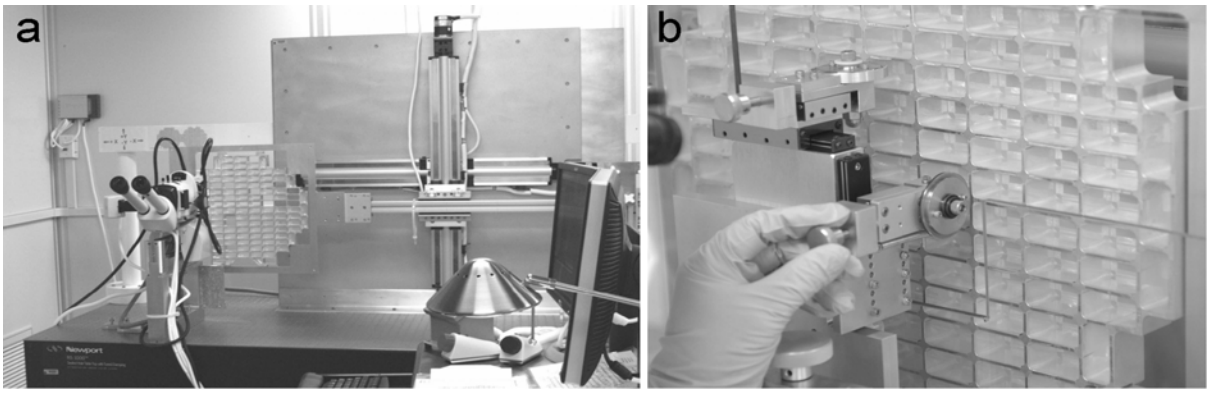

Fig. 2. a) The cometary collector mounted on a large scale, vertical x/y scanning platform, which in turn was fastened onto an air-cushioned optical bench, the latter accommodating the optical stereo-microscope and its CCD camera that were used for detailed imaging of all surfaces, as well as the tray-wide optical survey of all craters >20 μm in size. b) Foil-cutting apparatus with the double blade foil cutter in vertical position. The entire device was mounted on a series of mechanical slides that allowed precision x/y/z movements for alignment with any given tray rib. However, the curved edges of the foil concealed the exact position of the rib, such that it was not possible to harvest foil strips >1.7 mm wide.

Stardust craters described in this paper. The polydispersive nature of available fine glass bead samples, the difficulty of distinguishing inherent gun-derived debris impacts from craters generated by smaller projectiles, and technical problems in launching very small glass beads with known velocity characteristics in both light-gas and Van de Graaff accelerator guns have so far prevented accurate size calibration for smaller particles of soda-lime glass. We do not, therefore, have close experimental analogues for the smallest Stardust craters. However, the excellent statistical fit of the larger particle data to a linear calibration line, with a very small y-axis (crater top lip diameter) intercept of minus 0.7 ± 5.0 μm (Kearsley et al. 2006) suggests that the relationship should hold to micrometer-scale particles. Unfortunately, extensive detachment of the very thin crater lip, so commonly seen in these smaller craters (<20 μm in diameter), may lead to underestimation of the true top lip diameter. Comparison of diameter measurements, based on the true top lip and from the lip remnants after partial detachment suggests that their ratio is about 1:0.8, and thus the diameter may be underestimated by 25%. However, this may be partially offset by a decrease in the particle-to-crater diameter scaling relationship that we have recently determined for laboratory impacts by particles of 1.5 μm in diameter. The relationship between impactor size and crater size for particles of less than 1 μm in diameter remains unconfirmed, but as a first approximation, the relationship determined for larger events may be extended to these tiny features.

To correct the size calibration for variation in particle density, we use data from a further suite of experiments by Kearsley et al. (2007), who employed new projectiles of three different densities: 0.4 g cm^{-3} (hollow glass beads); 1.2 g cm^{-3} (polymethyl methacrylate); and 7.9 g cm^{-3} (stainless steel), spanning the range of density for likely cometary materials. From the top-lip diameter of these craters, additional calibration lines were drawn for low-density impactors, generating conversion factors that were used in the particle size fluence plots for Stardust of Hörz et al. (2006), although accurate calibration for small grains of high-density impactors (e.g., Fe Ni metal) will require further work. The density-dependent conversion factor described by the line in Fig. 3 of Kearsley et al. 2007 is:

$$\text{Crater top lip diameter/projectile diameter} = (1.91 \times \log_n (\text{projectile density g cm}^{-3})) + 2.90 \quad (1)$$

Along with craters from a range of polydispersive mineral powders with a range of grain shapes, the experimental craters were later subject to stereometric shape reconstruction, yielding internal crater diameter and depth below ambient plane data, from which the relationship between impactor density and crater depth/diameter could be determined, although with relatively poor precision. Nevertheless, impacts by materials with density less than 1.2 g cm^{-3} should be readily and unambiguously identified by their very shallow depth, and impact by a solid, low-porosity mafic silicate grain (e.g., Mg-rich olivine or pyroxene) should yield a crater with a top lip diameter 5 times the impactor diameter and a depth/diameter of about 0.6. In this paper, wherever it is possible to infer an impacting particle density and derive a particle diameter from a circular crater top-lip diameter, we have calculated values for grain diameter and mass as though the impactor were a spherical grain. Our most recent experiments have employed polydispersive wollastonite projectiles with elongate rod morphology (shot G190706#2) to investigate the role of silicate particle shape and impact aspect on crater depth/diameter ratio. We have also successfully fired about 400 μm aggregate projectiles made from mixed powders of San Carlos olivine, enstatite, Ca-rich pyroxene, chrome spinel, and pyrrhotite, bound with aerosol

polymer adhesive (shot G200207#2 onto a polished Al 6000 series alloy stub at 5.07 km s^{-1}) to simulate porous, low density aggregate impacts.

X-Ray Microanalysis Protocols

The complexity of X-ray microanalysis on particle residues in situ within impact craters has been discussed at length by Kearsley et al. (2007), who showed that coarse residues of common mafic silicate minerals in larger craters (>50 μm in diameter) usually retain characteristic element stoichiometry with only subtle changes, and can be identified easily. Focused ion beam preparation and transmission electron microscopy (FIB-TEM) and Raman studies of residue (e.g., Leroux et al. 2008; Burchell et al. 2008) have revealed crystalline residue in impact craters, but it is not yet possible to quantify survival of primary structure. During PE, it was necessary to employ two analytical different protocols, dependant on both the impact feature size and the instrumentation employed.

Large Craters (D > 20 μm Crater Top Lip Diameter)

The composition of relatively thick residue (>1 μm in thickness) in each large crater was determined using an Oxford Instruments INCA energy dispersive X-ray (EDX) spectrometer at NHM. All analyses were obtained at 20 keV (to promote high count rates for iron and nickel K alpha X-radiation) and 2 nA, at high vacuum except for the large crater on foil C107W,1, which was at 30 Pa pressure. The X-ray spectra for quantitative determination were taken from large patches of residue in the crater floor, with relative count rates suggesting that they are of close to micrometer-scale thickness, or in some cases several micrometers thick. Although major element ratios with a simple stoichiometric relationship of divalent cations to silicon may indicate residue derived from specific minerals, conventional SEM-EDX cannot determine how much diagnostic crystalline structure is present. It is also important to note that an apparent complexity of element ratios within a determination could be due to either a non-stoichiometric material, or a very fine-scale mixture of stoichiometric minerals, as the micrometer-scale interaction volume of the 20 kV electron beam can include X-ray emission from diverse nanometer-scale phases. This limits tentative identification of mineral precursors to those coarse (>3 micrometer) impact residues that show simple and constant element ratios across wide areas. Likewise, fine surface contamination may not be easily distinguished from underlying residue, although other sensitive non-destructive and high-resolution surface analysis techniques (such as Auger electron spectroscopy) may reveal heterogeneity in sub-micrometer elemental distributions. In this study, the exposed crater surfaces were rough and were not carbon-coated. Although the beam-sample-detector geometry, beam conditions and standards

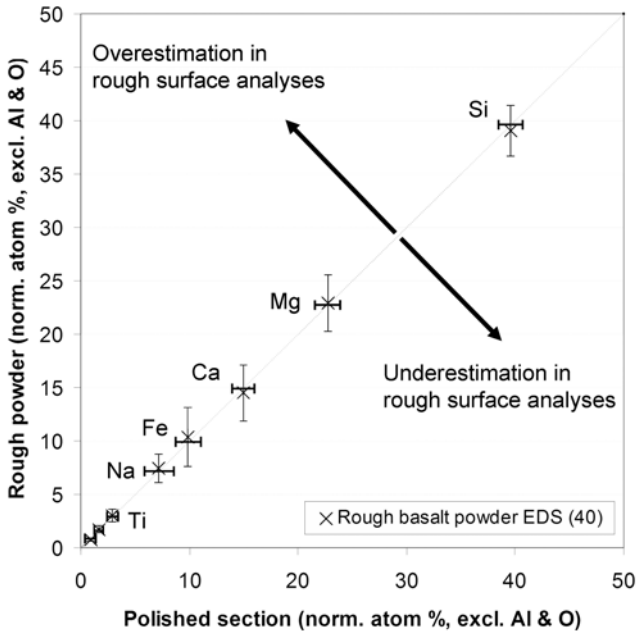

Fig. 3. Comparison of SEM-EDX analyses from polished basalt glass (X-axis and line) with those from rough basalt glass powder projectile surfaces (Y-axis and crosses). The plot shows atomic percentages normalized to a sum of 100%, after exclusion of Al and O (Al is not quantified in Stardust foil craters, and O is calculated by stoichiometry). Error bars are one standard deviation from the average. Note the much larger error bars for rough powder analyses.

(silicate, oxide, and sulfide minerals and metals) were close to those employed for routine quantitative analysis at NHM, the matrix corrections are approximate (see Kearsley et al. 2007). Wherever possible, the sample was tilted to allow electron beam incidence perpendicular to the residue surface (which permits the most appropriate matrix correction). The element abundances were calculated by comparison to the suite of NHM standards, and processed with an extended Pichou and Pouchoir (XPP) matrix correction, then normalized to 100%. Aluminum was excluded from the subsequent calculations because of the ubiquitous excitation of the Al foil substrate. Element abundances in this paper are expressed as wt% elements (Table 1) or oxides (Table 2), although S is present as a sulfide in some residue. Detection limits are similar to those for polished sections (less than 1% element weight for Z > 10, and for elements in the fourth row of the periodic table usually better than 0.5 wt%). Due to the spatial variation in the matrix path length before X-rays can escape from a rough surface, SEM-EDX analyses of residue may suffer from variable and unconstrained X-ray absorption. To establish typical levels of accuracy and precision that we might expect from rough crater residues, we have compared quantitative analyses taken from a polished microprobe section of USGS standard basalt glass NKT-1G with those from a loose powder of the same material (Fig. 3). Precision is noticeably poorer in the rough powder analyses, but

average determinations of the major elements still fall within 1 standard deviation of the polished section values, suggesting that our crater residue analyses of major elements are not seriously compromised.

Comparability of residue composition to pre-impact composition has also been described by Kearsley et al. (2007), and variable depletion of volatile elements such as sodium (Na) and sulfur (S) has been reported, e.g., Fig. S9 of the supplemental online materials (SOM) of Flynn et al. (2006). Analyses of coarse laboratory crater residues from pyroxenes and olivines of known composition have shown close matches to the projectile compositions when the correct beam incidence angle was achieved, although errors grew if the beam-specimen incidence angle was non-perpendicular (Kearsley et al. 2007). From these experimental results, it seems that mafic silicate mineral stoichiometry can be reliably recognized in coarser impact residues. However, a much wider scatter of apparent compositions may be observed in very thin residues and especially from small craters (Kearsley et al. 2007).

Small Craters (D < 20 μm)

Most of the numerous Stardust craters analyzed worldwide by SEM-EDX methods during PE were less than 20 μm in diameter. Similar experimental conditions were used by all groups measuring Stardust residue composition, with X-ray spectra obtained at 20 kV or 5 kV, and 2 nA current. In the case of micrometer- and sub-micrometer-sized craters, quantification cannot be taken as far as with larger craters. SEM-EDX analyses of residue on the rough floor of small experimental craters (less than 20 μm in diameter) gives very variable major element ratio data, suggesting wide scatter of apparent compositions, even where the mafic silicate projectile composition is well known and homogeneous (e.g., basalt glass impact residues in Fig. S10 of SOM for Flynn et al. 2006). This implies that quantification as element wt% is difficult, probably due to substantial matrix correction problems in very thin residues. Volatile elemental fractionation may also be more extensive, although analytical TEM of ultrathin sections cut by FIB (e.g., Graham et al. 2006) from similar small basalt craters usually shows little depletion even of sodium in the residue, suggesting that the in situ SEM-EDX analytical method may often be at fault, rather than major compositional change (Kearsley et al. 2007). The small size of the crater, with breadth and depth dimensions now comparable to the electron beam interaction volume for in situ SEM-EDX, also prevents spatial resolution of different composition materials by point analysis or mapping, and only an integrated analysis of the entire crater is possible. However, the recent use of Auger electron spectroscopy by Stadermann et al. (2007) has demonstrated a technique suitable for nanometer-scale, in situ, non-destructive elemental characterization of residue surfaces. The thickness of the melted residue in such a crater may be only a few tens of nanometers, although this may include both fragments and melt from discrete mineral phases, as demonstrated by FIB-TEM sections (Leroux et al. 2008). The much thinner residue in very small craters requires use of low accelerating voltage in SEM-EDX to concentrate X-ray excitation within the residue layer. Complex and very variable beam-specimen geometry across the crater not only makes matrix correction inaccurate, but the necessity of using strongly overlapped L family X-ray lines for transition metal determination (due to the low beam overvoltage) now restricts detection to major element concentrations. Impact experiments using volatile-rich projectiles also show there is very variable loss of elements such as sulfur, with greater depletion in smaller craters.

Two caveats should therefore be expressed in considering our analyses of craters: even under the best circumstances, crater residues may underestimate the original particle content of volatile elemental species such as sulfur; smaller craters may yield a useful representative inventory of the major elements present within residue, but their in situ SEM-EDX analyses may not give reliable elemental concentrations or stoichiometric ratios.

RESULTS

Crater Distribution, Size, and Shape

During PE, size and residue composition measurements were taken on seven large craters (top lip diameter >20 μm), and about 300 smaller craters (top lip diameter <20 μm). The locations of foils selected for detailed flux analysis (Hörz et al. 2006), and from which our examples of small craters are drawn, are shown in Fig. 4.

The sample of craters available for our study was identified in two separate parts of the PE:

a) A multi-institution survey of all craters on a suite of 23 foils, to establish a particle fluence, as reported in Hörz et al. (2006). The survey was carried out at low magnification (>200×) across ~10 cm^2 of foil, and on randomly chosen areas (totalling 2.85 cm^2) at high magnification (between 1000×, 2000×, and 5000×), yielding large numbers of sub-micrometer to 5 μm craters. The smallest crater recognized had a top lip diameter of 102 nm. More than 80% of the craters in the small size fraction were smaller than 5 μm, with only 13 craters between 5 and 20 μm. A large variation in the crater distribution was found at the mm^2 scale, with a range from 0 to more than 50 features identified per foil. Three foils (C008N, C020W, and C044N) are heavily cratered, holding about one-third of all the craters analyzed by SEM/EDX in this study. Furthermore, five foils (C037N, C044W, C052N, C055N, and C068W) each contain more than 10 craters, so that the eight "crater–clustered foils" contain ~85% of the total number of craters, in less than one-third of the

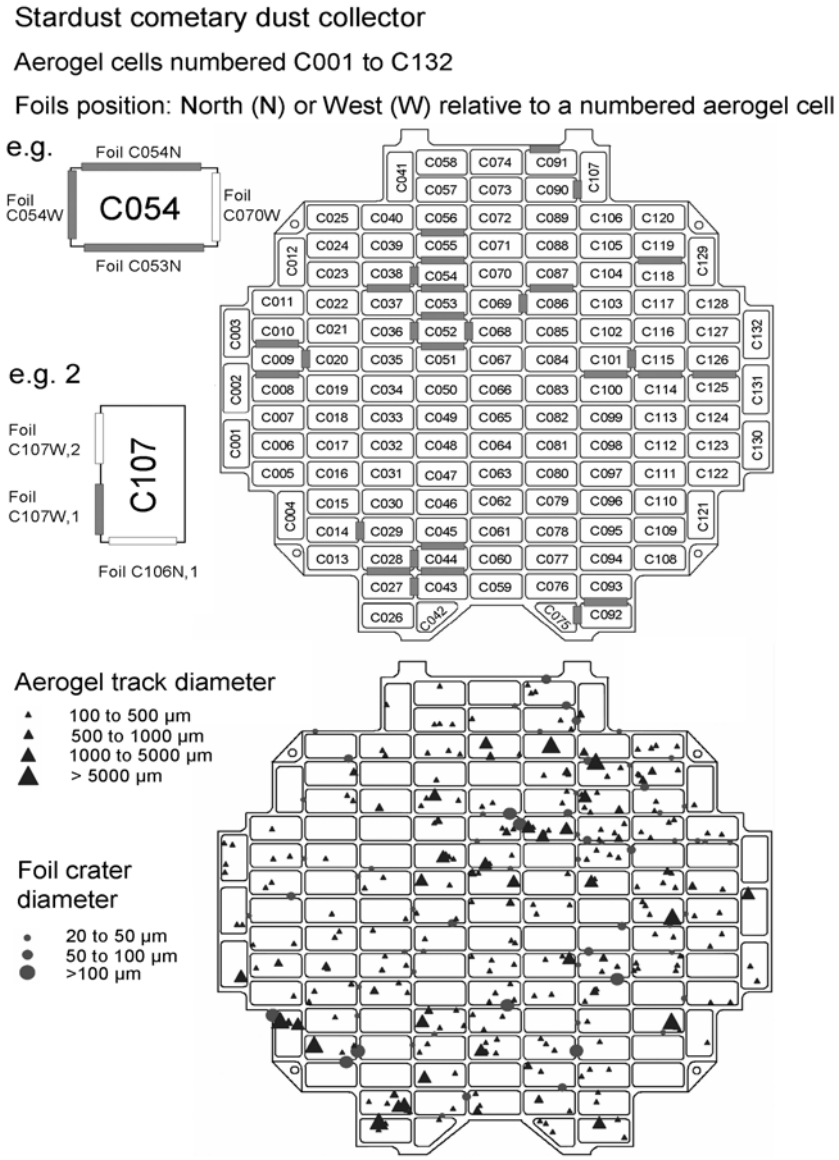

Fig. 4. a) Nomenclature for location of foils; those described in this paper are shown in gray. b) Impact locations and sizes of features on the Stardust cometary collector, determined by the initial optical survey at Johnson Space Center. Larger aerogel tracks are shown as black triangles; large craters are shown as gray circles with their diameter in micrometers given in the key. Figure modified from the supplemental online materials of Hörz et al. (2006).

scanned area. Possible causes for the highly heterogeneous spatial distribution of the small craters are discussed in Westphal et al. (2008).

b) Multi-technique analysis of large craters (exceeding 50 µm top-lip diameter), which are relatively rare on the collector, were specifically selected for detailed study during optical survey of the foils while still attached to the collector frame, and were subsequently harvested. These impact features were imaged and analyzed in a well-defined sequence of analytical protocols in different laboratories, involving time-of-flight secondary ion mass spectrometry (TOF-SIMS; Leitner et al. 2008); SEM-EDX; NanoSIMS (Hoppe et al. 2006; Stadermann et al. 2008); and in some cases, Raman spectroscopy and FIB-TEM (Graham et al. 2006; Leroux et al. 2006, 2008).

The following foils were surveyed for small crater identification by SEM; the number of craters analyzed by EDX on each foil (>80% of the total) is indicated in parentheses: C008N,1 (92); C020W,1 (33); C027N,1 (2); C037N,1 (19); C043N,1 (3); C043W,1 (5); C044N,1 (49); C044W,1 (13); C051N,1 (1); C052N,1 (11); C052W,1 (0); C053N,1 (4); C054N,1 (8); C054W,1 (9); C055N,1 (17); C060W,1 (1); C068W,1 (13); C092N,1 (3); C092W,1 (1); C100N,1 (2); C114N,1 (3); C115W1 (0) and C125N,1 (3).

Large craters were examined by analytical SEM on foils: C009N,1; C029W,1; C086N,1; C086W,1; C091N,1; C107W,1,4; and C118N,1.

Combining data from these two surveys, our sample includes a large number of very small craters (292) and a small number (7) of large craters. The area scanned at low magnification during PE represents approximately 10% of the total foil exposed to cometary dust impacts, but only a small proportion was surveyed at high magnification for the smallest craters. Also, although the number of small craters on the collector must be enormous (see Hörz et al. 2006), together they can contain only a very small proportion of the total dust mass collected, probably only ~1% of the total mass on the collector resides in craters of less than 5 μm in size. In contrast, the larger craters examined by SEM-EDX during PE (7 from 63 features >20 μm found in the optical survey) not only represent about 11% of the total number of similar craters on the collector, but may also contain ~10% of all the cometary dust mass collected on all of the foils.

Large Impact Features: Morphology and Residue Composition

Seven large craters were examined in detail, six having pristine morphology, but the largest one (C086W,1) having a torn and folded crater floor, probably due to impact-induced adhesion to the underlying Al frame and deformation during removal of the foil. Stereo anaglyphs, color-coded depth models, and vertical depth profiles are shown in Fig. 5. The attributes of each crater are described below in foil number sequence. Integrated bulk EDX analyses for each crater are tabulated in Table 1; representative point analyses of residues are tabulated in Table 2.

Table 1 is modified from Table S2 of SOM for Flynn et al. (2006), with the improved particle diameter and mass calibration of Kearsley et al. (2007) including density dependence correction, and with new analyses from optimum geometry. Crater names use the standard notation for foil location on the collector frame. Crater dimensions are top lip diameters (cf. Kearsley et al. 2006), with the crater inner diameter and depth now derived from MeX stereometric reconstructions. Morphology reflects either a single bowl or a field of overlapping (compound) craters. Analyses are averages of point spectra, collected for 50 s live time and typically yielding 75,000 X-ray counts, or area integrals extracted from spectral map data (of varying duration), all performed using an Oxford Instruments INCA EDX spectrometer on a JEOL 5900LV SEM, operating at 20kV and 2nA, at high vacuum. For example, the average for C086N,1 is based on 12 point analyses, and the whole-crater composition for C029W,1 is based on integration of X-ray data from across the floor of the feature. Detailed individual determinations can be found in Table 2. All analyzed crater surfaces were rough and with no carbon coat; matrix corrections are therefore approximate. Aluminum was included in the spectrum peak and background fitting routine, but was then subtracted from the analytical totals to account for ubiquitous excitation of the metal substrate, and results were normalized to 100%. Aluminum is therefore shown as not determined (nd), although it is likely to have been present even as a major element in some residues (e.g., the Ca-rich silicate residues of C029W,1 and C086W,1). Wherever possible, the sample was tilted to allow electron beam incidence perpendicular to the residue surface (Tilt), giving the best matrix corrections. Bulk determinations are shown in the table as element wt%. For this convention, all Fe and Ni were assumed as divalent cations, although some may be present as metal. Oxygen was calculated by stoichiometric association with other elements after subtraction of appropriate Fe and Ni, as though bound in simple stoichiometric sulfide (Fe + Ni:S = 1:1). However, experimental data of Kearsley et al. (2007) have already shown that real sulfide impact residue can be S-depleted, with diverse Fe and Ni to S ratios created by impact processing. Determinations of less than 3 times background variation are listed as "below detection limit" (bdl). If found above the detection limit in more than one determination for the crater, an element is listed as "trace." The ratio of the sum of the divalent cations (minus iron for notional FeS) to silicon is shown as "[Div]/Si." The ratio Mg:(Fe-S) is intended to show the major cation ratio in silicate, with appropriate Fe subtracted as though bound in FeS. Tentative identification of mineralogy in an original impactor component is suggested where multiple analyses yield evidence of stoichiometric relations considered typical of a particular mineral family: "Ol" denotes olivine, "Px" pyroxene, and "Su" sulfide. Suggested mineralogical attributions will require confirmation by analytical TEM, e.g., electron diffraction study. "Non-stoich" residue may be "mafic" (Ma) and/or "alkaline" (Ak) rich, and may be a mixture of nanometer stoichiometric phases. Estimated impactor mass for bowl-shaped craters was calculated from the top lip diameter relationship to impactor diameter (Kearsley et al. 2006), corrected for estimated density (Kearsley et al. 2007).

Stardust Foil C009N,1 (Fig. 6)

This foil segment contains a simple, bowl-shaped crater of ~64 μm top lip diameter, ~50 μm internal diameter, and ~30 μm depth below ambient plane, giving a depth/diameter ratio of 0.6. The crater is lined by abundant large patches of fragmental residue, some over 10 μm across, dominated by Mg-rich silicate, with a low Fe content (Table 2). Variable Cr may reflect either differences in silicate composition or a scattering of very small spinel-group oxides, although no evidence of high atomic number phases was seen in backscattered electron images of the residue. The divalent ion to silicon ratio is approximately 2.8:2, suggesting that the silicate is not a remnant of simple monomineralic olivine or Mg pyroxene, but could be either a very fine-grained mixture

Table 1. Summary of bulk residue composition in Stardust foil craters of greater than 50 μm diameter, expressed as element wt%.

Crater	C009N,1	C029W,1	C086N,1	C086W,1	C091N,1	C107W,1	C118N,1
Morphology	Bowl	Compound	Bowl	Bowl?	Compound	Bowl	Bowl
Top lip diameter (μm)	64	167 × 133 irregular	57	295	62	85	68
Diameter on ambient (μm)	50.6	142	43.6	~235?	55.0	62.6	55.0
Depth below ambient (μm)	32.9	34.1	33.8	>165?	24.8	36.1	31.0
Method	Normal EDX	Normal EDX	Tilt EDX	Tilt EDX	Normal EDX	Tilt EDX	Tilt EDX
Normalized wt%	Average of 4 point analyses	Whole crater, EDX spectra extracted from map	Average of 12 point analyses	20 × 20 μm square area integrated	Average of 5 point analyses	Average of 12 point analyses	Average of 8 points and 1 area analyses
Na	bdl	1.2	bdl	1.5	bdl	0.0	4.4
Mg	25.1	11.1	33.4	16.5	24.2	18.7	12.3
Al	nd	nd	nd	nd	nd	nd	nd
Si	22.3	11.1	19.4	16.9	21.8	24.9	24.3
P	0.0	0.0	0.0	0.1	0.0	0.0	0.3
S	0.5	13.9	Trace	0.7	Trace	0.0	1.5
Cl	bdl	bdl	bdl	bdl	bdl	Trace	0.5
K	bdl	bdl	bdl	Trace	bdl	bdl	0.7
Ca	0.1	0.9	bdl	0.7	bdl	0.9	1.9
Ti	bdl	bdl	bdl	bdl	bdl	bdl	Trace
Cr	0.6	0.6	0.3	0.1	Trace	0.4	0.3
Mn	bdl	bdl	bdl	0.4	bdl	0.4	0.9
Fe	7.4	32.7	2.1	24.8	10.3	10.3	10.3
Ni	bdl	4.1	bdl	0.2	bdl	bdl	0.9
O	44.1	24.5	44.8	38.0	43.7	44.3	41.5
Comment	Cr variable from below detection limit up to 2.1 wt%	Polymineralic, much Fe and S together. Al with Na. Mg, Si, and Ca	All analyses across crater floor are very similar	Analyses on top lip. 3 phase, mix. K reaches 0.5 wt%	Analyses on top lip of crater. Cr varies from bdl to 0.8 wt%	Analyses on top lip of crater. Trace Cl?	Auger suggests two silicates and Ca in discrete oxide phase?
[Div]/Si	1.49	1.0	2.0	2.0	1.6	1.1	0.8
Mg:(Fe-S)	8.6	35.8	36.5	2.1	6.4	4.2	3.3
Possible mineralogy	Unknown	Px, Su, and non-stoich Ma	Ol (Fo 97)	Ol (Fo 65) + non-stoich Ak	Unknown	Unknown	Non-stoich Ma/Ak
Est. mass (ng)	3.5	17	2.5	344	3.2	8.2	4.2

Table 2. Individual spot analyses of residues in large Stardust foil craters for comparison with the average values of Table 1; note the substantial compositional variation for individual residue locations. All samples were craters in rough, uncoated foils, determined by EDX at NHM, using the protocols of Kearsley et al. (2007). Determinations are expressed as normalized oxide wt% (except discrete sulfides), with Al omitted due to ubiquitous Al excitation from the underlying metal substrate. Detection limits are defined as 3 times the standard deviation of the background; "bdl" denotes below detection limit for this element in this spectrum. Numbers of cations are calculated for 24 or 7 oxygens. Sulfide atoms are shown as a percentage. The Mg proportion in silicate is calculated for Fe corrected by removal of 1 Fe atom for each S atom found in the analysis. This may be a poor estimate in thinner residue due to excitation of Fe inclusions in the alloy substrate and loss of S from very small particles. Where cation ratio to 24 oxygen atoms is close to a typical stoichiometric value for a mafic silicate mineral, it is shown in bold. If not close to integer value for O = 24, stoichiometry is shown recalculated for 7 oxygen atoms.

	C009N,1		**C029W,1**										
	Area b			Area c		Area d			Area e				
	ak060427a		ak060519cc	ak060519c	ak060523f	ak060523f				ak060519	ak060519		ak060524a
Oxide			BEI2	BEI		Site 2			**Element**	BEI2	BEI		Site 4
wt%	**sp9**	**sp10**	**sp4**	**sp 7**	phase 2	**sp 11**	**sp 12**	**sp 13**	**wt %.**	**sp6**	**sp2**	**sp3**	**sp1**
Na_2O	bdl	bdl	bdl	1.5	1.0	3.3	3.9	bdl	Na	bdl	bdl	bdl	bdl
MgO	38.1	42.9	35.8	26.2	24.5	17.4	17.6	21.5	Mg	bdl	bdl	bdl	bdl
SiO_2	47.4	48.6	56.1	58.7	57.0	27.8	29.7	28.4	Si	bdl	bdl	bdl	bdl
P_2O_5	bdl	bdl	bdl	bdl	bdl	bdl	bdl	bdl	P	bdl	bdl	bdl	bdl
SO_3	0.8	bdl	4.4	2.6	3.5	27.8	28.8	27.6	S	33.0	35.2	36.4	37.8
K_2O	bdl	bdl	bdl	bdl	bdl	bdl	bdl	bdl	K	bdl	bdl	bdl	bdl
CaO	bdl	bdl	bdl	6.0	5.4	1.7	1.9	1.6	Ca	bdl	bdl	bdl	bdl
TiO_2	bdl	bdl	bdl	bdl	bdl	bdl	bdl	bdl	Ti	bdl	bdl	bdl	bdl
Cr_2O_3	3.1	bdl	bdl	bdl	0.8	bdl	bdl	bdl	Cr	bdl	bdl	bdl	bdl
MnO	bdl	bdl	bdl	bdl	bdl	bdl	bdl	bdl	Mn	bdl	bdl	bdl	bdl
FeO	10.7	8.5	3.7	5.0	7.7	20.4	18.1	20.9	Fe	60.6	38.2	57.4	56.4
NiO	bdl	bdl	bdl	bdl	bdl	1.6	bdl	bdl	Ni	6.4	26.6	6.2	5.8
Total	100.0	100.0	100.0	100.0	100.0	100.0	100.0	100.0	Total	100.0	100.0	100.0	100.0
Stoichiometry								**Atom%**					
Na				0.4	0.3	1.7	2.0						
Mg	8.2	9.1	7.7	5.6	5.4	6.9	6.9	8.2					
Si	6.9	6.9	8.1	8.4	8.4	7.4	7.8	7.3					
S	0.1		0.4	0.3	0.4	5.1	5.2	4.8	S	46.3	49.1	50.0	51.5
Ca				0.9	0.9	0.5	0.5	0.4					
Cr	0.4				0.1								
Fe	1.3	1	0.5	0.7	1.0	5.7	5.1	5.6	Fe	48.3	30.6	45.3	44.1
Ni						0.3			Ni	4.9	20.3	4.7	4.3
O (stoich)	24	24	24	24	24	24	24	24	Fe+Ni/S	1.15	1.04	1.00	0.94
O/Si	3.5	3.5	3.0	2.8	2.9	3.2	3.1	3.3	Fe/S	1.04	0.62	0.91	0.86
Cations:Si	1.4	1.5	1.1	0.9	1.0	2.7	2.5	2.6	Ni/S	0.1	0.4	0.1	0.1
Mg/(Mg + Fe)	0.86	0.90	0.93	0.89	0.84	0.55	0.57	0.60					
O = 7/Si	**2.01**	**2.01**											
O/Cations	**2.89**	**2.95**											

Table 2. *Continued.*

	C086N,1													
Oxide	1	2	3	4	5	6	7	8	9	10	11	12		
wt%													Avg	Stdev
Na_2O	bdl	bdl	bdl	bdl	bdl	bdl	bdl	bdl	bdl	bdl	bdl	bdl		
MgO	55.4	55.8	54.8	55.6	54.6	55.2	55.5	55.5	56.2	56.3	55.4	56.2	55.5	0.5
SiO_2	42.2	42.0	42.1	41.8	42.2	42.4	42.5	41.9	40.7	40.4	42.1	40.9	41.8	0.7
P_2O_5	bdl	bdl	bdl	bdl	bdl	bdl	bdl	bdl	bdl	bdl	bdl	bdl		
SO_3	bdl	bdl	bdl	bdl	bdl	bdl	bdl	bdl	bdl	bdl	bdl	bdl		
K_2O	bdl	bdl	bdl	bdl	bdl	bdl	bdl	bdl	bdl	bdl	bdl	bdl		
CaO	bdl	bdl	bdl	bdl	bdl	bdl	bdl	bdl	bdl	bdl	bdl	bdl		
TiO_2	bdl	bdl	bdl	bdl	bdl	bdl	bdl	bdl	bdl	bdl	bdl	bdl		
Cr_2O_3	bdl	bdl	bdl	bdl	bdl	bdl	bdl	bdl	bdl	bdl	bdl	bdl		
MnO	bdl	bdl	bdl	bdl	bdl	bdl	bdl	bdl	bdl	bdl	bdl	bdl		
FeO	2.5	2.2	3.1	2.6	3.2	2.4	2.0	2.6	3.1	3.3	2.5	2.9	2.7	0.4
NiO	bdl	bdl	bdl	bdl	bdl	bdl	bdl	bdl	bdl	bdl	bdl	bdl		
Total	100.0	100.0	100.0	100.0	100.0	100.0	100.0	100.0	100.0	100.0	100.0	100.0	100.0	
Stoichiometry														
Mg	11.7	11.8	11.6	11.8	11.6	11.7	11.7	11.8	12.0	12.0	11.7	12.0	11.8	0.1
Si	6.0	6.0	6.0	5.9	6.0	6.0	6.0	6.0	5.8	5.8	6.0	5.8	5.9	0.1
Fe	0.3	0.3	0.4	0.3	0.4	0.3	0.2	0.3	0.4	0.4	0.3	0.3	0.3	0.1
total	24	24	24	24	24	24	24	24	24	24	24	24	24.0	
O/Si	4.00	4.03	4.00	4.04	3.99	3.99	3.98	4.03	4.12	4.14	4.01	4.10	4.0	0.1
Cations:Si	2.01	2.03	2.00	2.04	1.99	1.99	1.98	2.03	2.12	2.14	2.01	2.10	2.0	0.1
Mg/(Mg + Fe)	0.98	0.98	0.97	0.97	0.97	0.98	0.98	0.97	0.97	0.97	0.97	0.97	0.97	0.00

Table 2. *Continued.*

	C086W,1											C091N,1				
Oxide	ak060419a	ak060420a site 4							ak060419a							
wt%	site4 sp3	sp2	sp3	sp4	sp5	sp6	sp7	sp8	sp10	sp11	sp12					
Na_2O	bdl	bdl	bdl	bdl	bdl	bdl	0.6	17.4	9.8	6.9	6.5	bdl	bdl	bdl	bdl	bdl
MgO	25.3	24.5	28.8	28.5	29.7	30.0	26.0	5.0	9.4	9.3	9.9	40.3	42.4	42.7	40.8	42.3
SiO_2	36.5	39.7	37.9	38.0	39.4	38.9	37.7	65.3	54.8	53.0	48.8	46.9	45.8	45.4	45.7	47.9
P_2O_5	bdl	bdl	bdl	bdl	bdl	bdl	bdl	0.4	2.4	1.4	2.5	bdl	bdl	bdl	bdl	bdl
SO_3	0.6	bdl	bdl	1.3	bdl	bdl	0.6	0.8	1.9	1.2	0.4	bdl	bdl	bdl	bdl	bdl
K_2O	bdl	bdl	bdl	bdl	bdl	bdl	bdl	0.6	0.4	0.2	0.2	bdl	bdl	bdl	bdl	bdl
CaO	0.3	0.3	0.2	0.2	0.2	0.3	0.5	2.3	8.9	11.3	13.0	bdl	bdl	bdl	bdl	bdl
TiO_2	bdl	bdl	bdl	bdl	bdl	bdl	bdl	0.3	1.2	1.6	2.3	bdl	bdl	bdl	bdl	bdl
Cr_2O_3	0.3	bdl	0.3	0.3	0.3	0.2	bdl	bdl	bdl	bdl	bdl	0.9	0.6	0.4	bdl	bdl
MnO	0.5	0.6	0.4	0.5	0.3	0.5	0.6	bdl	0.4	bdl	0.3	bdl	bdl	bdl	bdl	bdl
FeO	36.4	35.0	32.5	31.2	30.0	30.1	34.1	8.1	10.8	15.1	16.1	12.0	11.2	11.5	13.5	9.8
NiO	bdl	bdl	bdl	bdl	bdl	bdl	bdl	bdl	bdl	bdl	bdl	bdl	bdl	bdl	bdl	bdl
Total	100.0	100.0	100.0	100.0	100.0	100.0	100.0	100.0	100.0	100.0	100.0	100.0	100.0	100.0	100.0	100.0
Stoichiometry																
Na							0.2	4.8	2.8	2.0	1.9					
Mg	6.3	6.0	7.0	6.9	7.1	7.2	6.4	1.1	2.1	2.1	2.3	8.7	9.2	9.3	8.9	9.1
Si	6.1	6.5	6.2	6.1	6.3	6.3	6.2	9.4	8.1	8.0	7.5	6.8	6.7	6.6	6.7	6.9
P									0.3	0.2	0.3					
S	0.1			0.2			0.1	0.1	0.2	0.1	0.1					
K								0.1	0.1							
Ca	0.1	0.1					0.1	0.3	1.4	1.8	2.1					
Ti									0.1	0.2	0.3					
Cr												0.1	0.1	0.1		
Mn	0.1	0.1	0.1	0.1		0.1	0.1									
Fe	5.1	4.8	4.4	4.2	4.0	4.1	4.7	1.0	1.3	1.9	2.1	1.5	1.4	1.4	1.7	1.2
Oxygen	24	24	24	24	24	24	24	24	24	24	24	24	24	24	24	24
O/Si	**3.9**	**3.7**	**3.9**	**3.9**	**3.8**	**3.8**	**3.9**	2.6	3.0	3.0	3.2	3.52	3.60	3.63	3.58	3.49
Cations:Si	**1.9**	**1.7**	**1.9**	**1.8**	**1.8**	**1.8**	**1.8**	0.2	0.6	0.7	0.9	1.51	1.60	1.62	1.58	1.49
Mg/(Mg + Fe)	1.26	1.24	1.58	1.69	1.76	1.78	1.38	1.20	1.84	1.18	1.13	0.86	0.87	0.87	0.84	0.89
O = 7/Si												**1.99**	**1.94**	**1.93**	**1.96**	**2.01**
O/Cations												**2.98**	**3.08**	**3.11**	**3.08**	**2.98**

Table 2. *Continued.*

	C107N,1											C118N,1						
Oxide	Lip		Floor						Al 17%	45%	80%							
wt%	1	2	1	2	3	4	5		7	17	20	2	3	4				
Na	bdl	bdl	bdl	bdl	bdl	bdl	bdl	bdl	bdl	bdl	bdl	5.6	6.5	5.1	6.3	5.8	5.9	5.1
Mg	29.9	31.4	31.6	33.5	35.9	34.4	38.3	29.0	38.2	32.0	22.1	20.1	18.4	17.0	19.7	25.4	22.9	18.9
Si	50.5	50.6	51.8	51.7	46.5	51.5	45.9	47.8	45.7	52.8	27.9	54.6	52.1	53.3	55.8	48.7	51.5	53.7
P	bdl	bdl	bdl	bdl	bdl	bdl	bdl	0.7	bdl	bdl	bdl	bdl	0.9	bdl	bdl	bdl	bdl	0.7
S	0.6	bdl	0.7	0.4	0.7	0.7	bdl	bdl	bdl	bdl	bdl	3.5	2.5	6.0	bdl	3.5	2.3	2.5
K	bdl	bdl	bdl	bdl	bdl	bdl	bdl	bdl	bdl	bdl	bdl	1.3	1.3	1.9	1.0	bdl	bdl	0.7
Ca	1.3	1.5	1.1	1.1	0.7	1.0	0.4	1.7	0.4	1.1	2.0	2.3	2.1	1.7	6.4	2.0	2.4	1.6
Ti	bdl	bdl	bdl	bdl	bdl	bdl	bdl	bdl	bdl	bdl	bdl	bdl	bdl	bdl	bdl	bdl	bdl	bdl
Cr	4.2	0.8	0.6	0.5	bdl	0.4	bdl	2.0	bdl	0.5	bdl	bdl	bdl	bdl	1.2	bdl	bdl	bdl
Mn	bdl	bdl	bdl	0.4	0.5	bdl	bdl	0.8	0.5	bdl	2.9	bdl	bdl	bdl	bdl	1.3	1.6	1.6
Fe	13.5	15.7	14.3	12.5	15.7	12.1	15.4	18.0	15.3	13.7	45.0	12.6	16.1	14.9	9.5	13.2	13.3	15.2
Ni	bdl	bdl	bdl	bdl	bdl	bdl	bdl	bdl	bdl	bdl	bdl	bdl	bdl	bdl	bdl	bdl	bdl	bdl
Total	100	100	100	100	100	100	100	100	100	100	100	100	100	100	100	100	100	100
																	Cl 0.7	Cl 0.9
Stoichiometry																		
Na												1.6	1.8	1.4	1.8	1.7	1.7	1.4
Mg	6.6	6.9	6.9	7.2	8.0	7.4	8.5	6.5	8.4	6.9	6.0	4.3	4.0	3.7	4.3	5.5	5.0	4.1
Si	7.4	7.4	7.6	7.5	7.0	7.5	6.8	7.2	6.8	7.6	5.1	7.9	7.7	7.7	8.2	7.1	7.6	7.9
P								0.1					0.1					0.1
S	0.1		0.1		0.1	0.1						0.4	0.3	0.7		0.4	0.3	0.3
K												0.2	0.3	0.4	0.2			0.1
Ca	0.2	0.2	0.2	0.2	0.1	0.1	0.1	0.3	0.1	0.2	0.4	0.3	0.3	0.3	1.0	0.3	0.4	0.2
Cr	0.5	0.1	0.1	0.1				0.2		0.1	0.0				0.1			
Mn				0.1	0.1			0.1	0.1		0.4					0.2	0.2	0.2
Fe	1.7	1.9	1.8	1.5	2.0	1.5	1.9	2.3	1.9	1.6	6.9	1.5	2.0	1.8	1.2	1.6	1.6	1.9
Oxygen	24	24	24	24	24	24	24	24	24	24	24	24	24	24	24	24	24	24
O/Si	3.23	3.23	3.17	3.20	3.45	3.21	3.54	3.35	3.54	3.15	4.69	3.05	3.14	3.12	2.94	3.37	3.17	3.06
Cations:Si	1.21	1.23	1.18	1.20	1.47	1.22	1.54	1.32	1.54	1.15	2.69	1.06	1.15	1.06	1.05	1.36	1.21	1.06
Mg/(Mg + Fe)	0.80	0.78	0.80	0.83	0.80	0.83	0.82	0.74	0.82	0.81	0.47	0.74	0.67	0.67	0.79	0.77	0.75	0.69
O = 7/Si	2.17	2.17	2.21	2.19	**2.03**	2.18	**1.98**	2.09	**1.98**	2.22	1.49							
O/Cations	2.40	2.56	2.52	2.55	**2.91**	2.60	**3.02**	2.55	**3.01**	2.49	3.77							

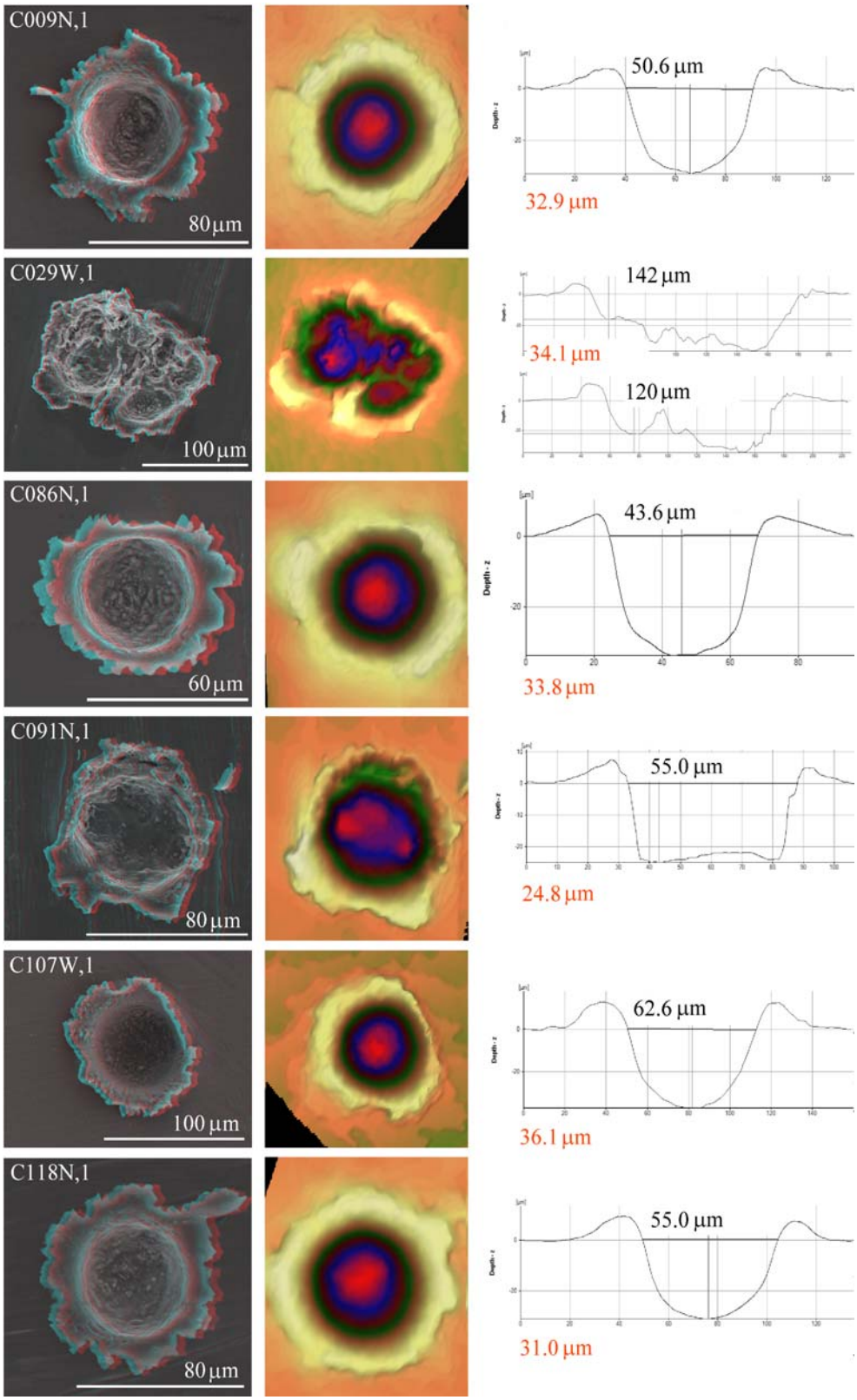

Fig. 5. Six large Stardust craters. Stereo anaglyph images (left eye red, right eye green), digital depth models (deepest part in red), and vertical depth profiles. The internal crater diameter on the ambient plane is shown in black numbers and the maximum depth below the ambient plane in red numbers. The vertical depth profiles give an accurate surface shape, but cannot show the cavity beneath the thin overturned crater lip as this was out of the line of sight for the electron images, and it is therefore rendered as though a solid lip.

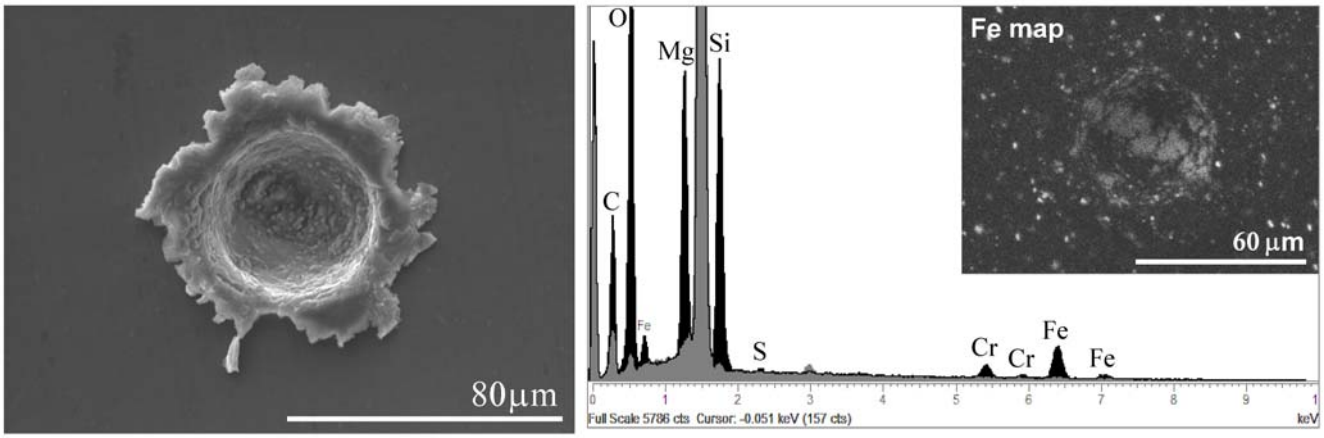

Fig. 6. C009N,1 SEI of crater; ED X-ray spectrum of silicate-dominated residue taken from a prominent patch on the crater floor, rich in Mg with Fe, Cr, and S (residue in black, substrate in gray); and Fe X-ray map to show distribution of coarse residue.

of almost equal parts of both olivine and pyroxene (pyroxene slightly in excess), or a non-stoichiometric material such as a glass. Traces of S also occur in places. Further interpretation of this crater will require FIB preparation and TEM analysis of residue to determine crystallography of any remnant impactor. Assuming density to be ~3.2 g cm^{-3} (derived from crater depth/diameter), the particle responsible for this crater was probably about 13 μm in diameter, with a total mass of ~3.5 ng.

Stardust Foil C029W,1 (Fig. 7)

This feature is a broad, shallow, and irregular patch of overlapped craters extending across 167 μm, with more than 12 individual component depressions of varying depth (between 20 and 40 μm below the foil ambient plane). There are no other foil impact features within several millimeters of this complex feature, and only one other, small circular crater on the same short foil. Stereo images and DEM depth models of the complex feature show that the depressions have partial circular outlines, apparently overprinted and deformed by each other. The vertical depth profiles reveal that most depressions lack true overturned rims, although they may be separated by uplifted septa. As this complex, compound impact feature cannot be explained simply by reference to the processes responsible for craters with bowl morphology, we defer discussion of the impacting particle size, structure, and overall composition to the final part of this paper where we consider criteria for recognition of aggregate impactors with heterogeneous internal density distribution. EDX maps (Fig. 7) show that the residue composition differs from one depression to another. The most abundant components (Fig. 8) are dispersed and very fine-grained Mg Fe silicate with S and minor Na and Ca; four discrete 3 μm grains of Mg silicate (with a stoichiometry like that of Mg pyroxene; see Table 2); patches of Ca-rich Mg silicate up to 5 μm across (with cation to silicon ratio suggesting possible

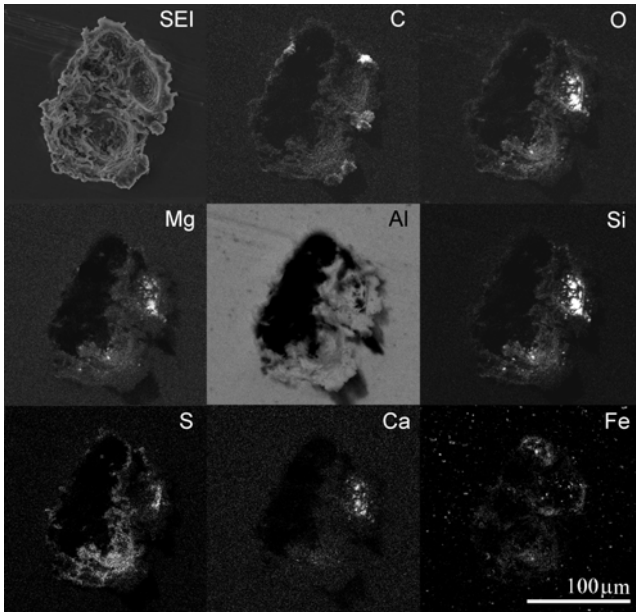

Fig. 7. Secondary electron image and X-ray maps of residues in a large impact feature on C029W,1. X-ray detector is to the top left, hence the shadow effect. Note the abundant Fe-rich inclusions in the Al alloy surrounding the crater.

derivation from clino-pyroxene; Table 2); 1–3 μm Fe-, Ni-, and S-rich particles spread across a 30 μm wide patch (probably sulfides); and C-rich material in one depression and in patches around the crater rim. The patchy fine-grained layer rich in Fe, S, and Mg silicate residue is found throughout the craters, with X-ray spectra dominated by Al (>90% of total counts) indicating a very thin, discontinuous sheet, possibly solidified melt, and probably less than 1 μm in depth. Carbon-rich patches revealed by EDX maps of the crater rim (Fig. 7), occur in the same areas that yield high ^{1}H-, ^{12}C-, and CH- ion signatures in TOF-SIMS (e.g., Leitner et al. 2008). Initial SEI (e.g., Fig. 8) also showed circular

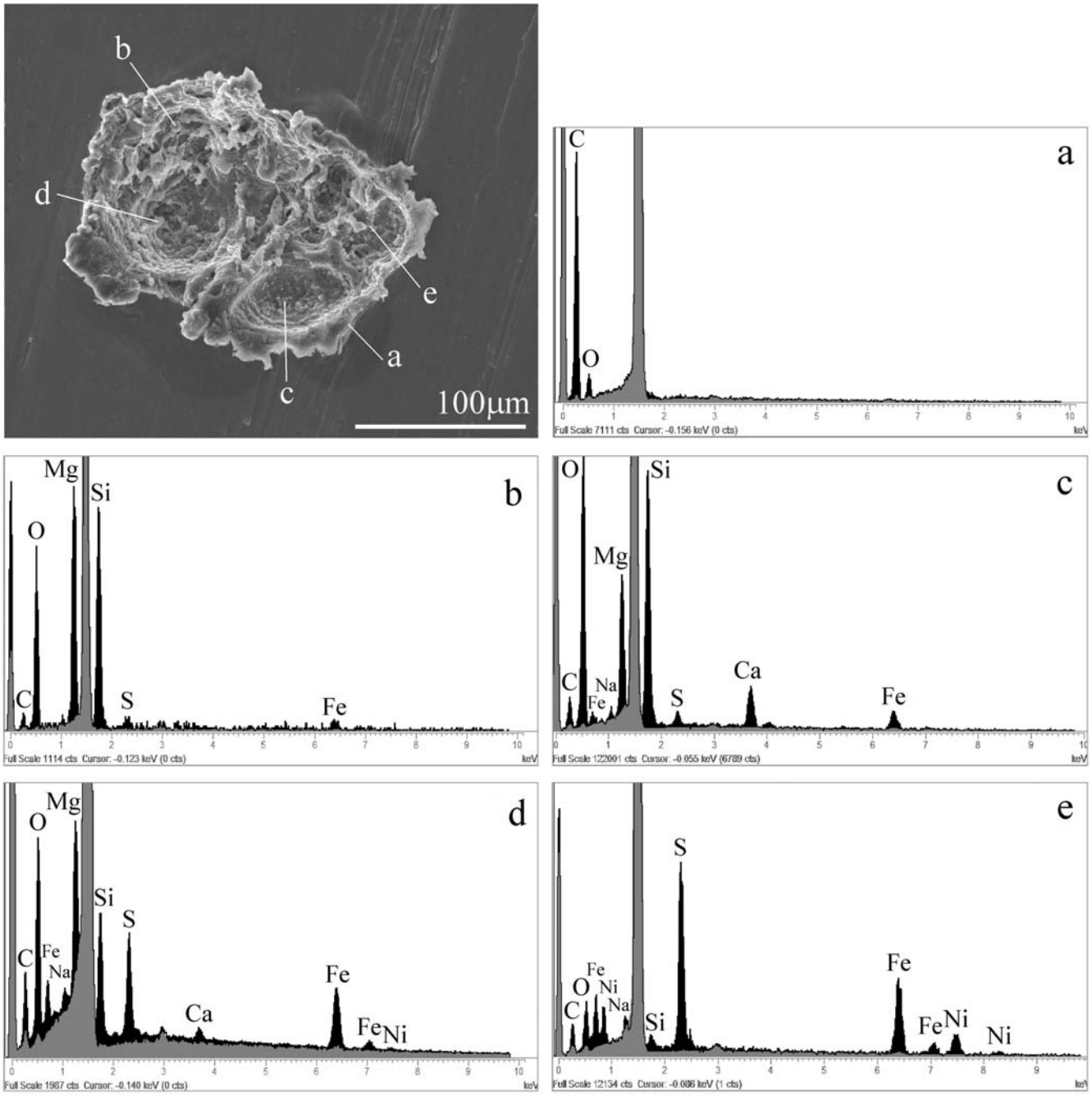

Fig. 8. C029W,1 SEI of impact feature showing location of ED X-ray spectra of residues in different parts of the feature. Note the darker areas immediately outside the crater. Residue spectrum is in black; substrate is in gray.

patches of suppressed secondary electron generation around these areas of the crater, as is also often seen to surround very small craters.

Stardust Foil C086N,1 (Fig. 9)

This foil has a simple bowl-shaped crater of 57 μm top lip diameter, although it is relatively deep with a depth/diameter ratio (0.78), which is greater than the majority of silicate impactors. We discuss this anomalous depth/diameter ratio in the context of our recent work on impacting particle shape in the final part of this paper. The crater appears to be due to an impact by a single dense grain dominated by one mineral species. Abundant coarse residue patches on the crater floor, each 3–5 μm across, are Mg-rich silicate, and all analyses of residue by EDX are very similar (12 analyses in Table 2), showing a stoichiometry of Mg + Fe:Si to be almost exactly 2:1, strongly suggesting an olivine impactor. The Mg to Fe ratio is equivalent to composition of approximately ~97.5%

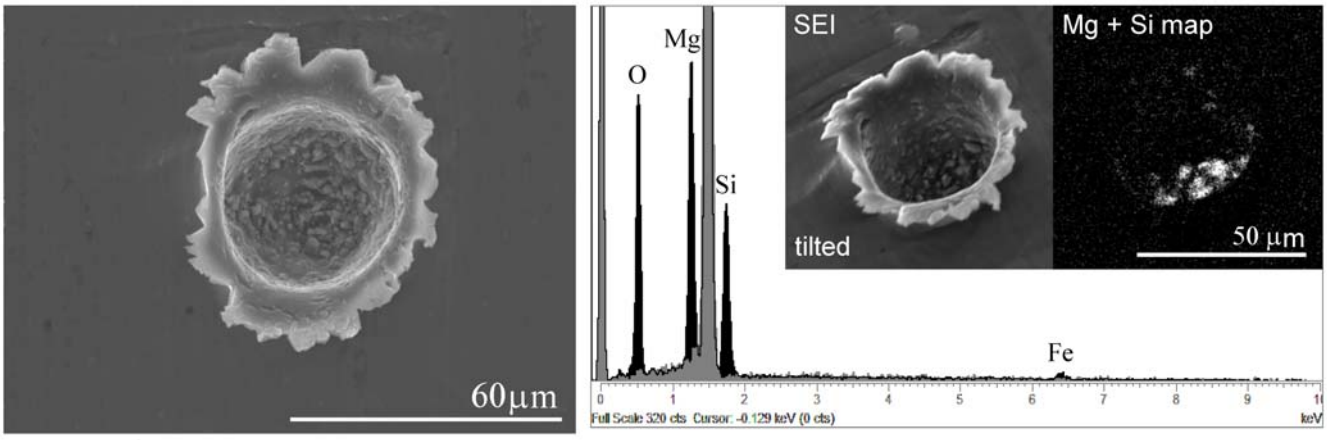

Fig. 9. C086N,1 SEI of crater; typical ED X-ray spectrum of residue; tilted SEI and Mg + Si X-ray map showing coarse (>micrometer-scale) fragments on crater floor. Residue spectrum is in black; substrate is in gray.

forsterite. Carbon, nitrogen, and oxygen isotopic analyses for this crater are described in Stadermann et al. (2008). Crater top-lip diameter calibration, density scaled for 3.2 g cm^{-3} suggests a particle diameter ~11 μm, and mass ~2.5 ng.

Stardust Foil C086W1 (Fig. 10)

This foil contains the largest crater analyzed during the PE, and has been deformed by detachment from the underlying frame, resulting in tearing of the thin foil remnant on the crater floor, lateral stretching of the lower crater wall, rupturing, and overturning of one wall. Full thickness foil penetration and impact on the corner of the underlying frame may have propelled some of the impactor into the neighboring aerogel block. From measurement of the remaining rim circumference, an original top lip diameter of ~295 μm can be deduced. Residue in this crater is very abundant, covering over 15% of the visible crater interior as scattered patches up to 20 μm across and 3 μm in thickness (Fig. 11). The most abundant residue is Mg Fe silicate with low but detectable Mn and Cr, for which numerous analyses (e.g., the first seven analyses for this crater in Table 2) give a divalent ion (Mg + Ca + Cr + Mn + Fe-S) to silicon ratio of ~2, suggesting that the impacting particle may have been dominated by an olivine precursor, with relatively high iron content at forsterite 65% fayalite 35%. In a few locations, the residue is highly heterogeneous at the micrometer scale, comprising an intimate mixture of small, rare Fe- and S-rich grains and two silicate components: the Mg Fe silicate described above (which dominates), and lesser quantities of a second silicate that is rich in Na and Ca, with substantial variation in the Na:Ca ratio. Phosphorus, S, K, and Ti are all present above detection limit in this material, which is probably also Al-rich, although this cannot be proven in SEM-EDX of the rough crater surface due to the Al1145 substrate beneath. Subsequent NanoSIMS mapping of a large heterogeneous residue patch (in the white box of Fig. 10) revealed a small grain with anomalous oxygen isotopes ratios indicative of a pre-solar origin (McKeegan et al. 2006; Stadermann et al. 2008). Although we were unable to perform full stereometric reconstruction of the original crater shape due to the complex deformation, our depth model shows that the depth clearly extended through the full foil thickness, and was probably in excess of 165 μm in depth, with a thin remnant of foil stretched over a shallow depression in the underlying collector frame. From the plan-view optical microscope images taken prior to de-integration and the shape of the remaining feature on the foil, we can infer that the complete, undisturbed crater probably had a circular bowl-shaped morphology, albeit with a relatively flat floor. The estimated depth/diameter ratio is in excess of 0.6 (an approximate figure, with the crater internal diameter assumed as ~80% of the estimated top lip diameter, as observed in our experimental craters). The particle responsible may therefore have had a density between 2 and 4 g cm^{-3}, which is typical of solid silicates with low porosity (Kearsley et al. 2007). The likely size of the impactor is ~59 μm in diameter and ~344 ng in mass.

Stardust Foil C091N,1 (Fig. 12)

This foil holds a 62 μm top-lip diameter structure of complex and rather odd, flat-bottomed shape (Fig. 5), although it is not sufficiently deep to reach the full foil thickness (where a flat-bottomed base is seen to be common in experimental impacts). With an internal diameter of 55.0 μm and maximum depth of 24.8 μm, the depth/diameter ratio is low (0.45). In plan view, the feature appears to be a composite of at least two overlapped larger craters, plus overlain smaller depressions. The stereometric depth model indicates possibly three small bowl-shaped impact features superimposed on two larger, near-perfectly registered larger craters. Residue is abundant on the floor, walls and lip, and shows very similar ED X-ray spectra throughout, comprising Mg silicate and small patches of Fe sulfide. The Mg + Fe:Si ratio determined from multiple

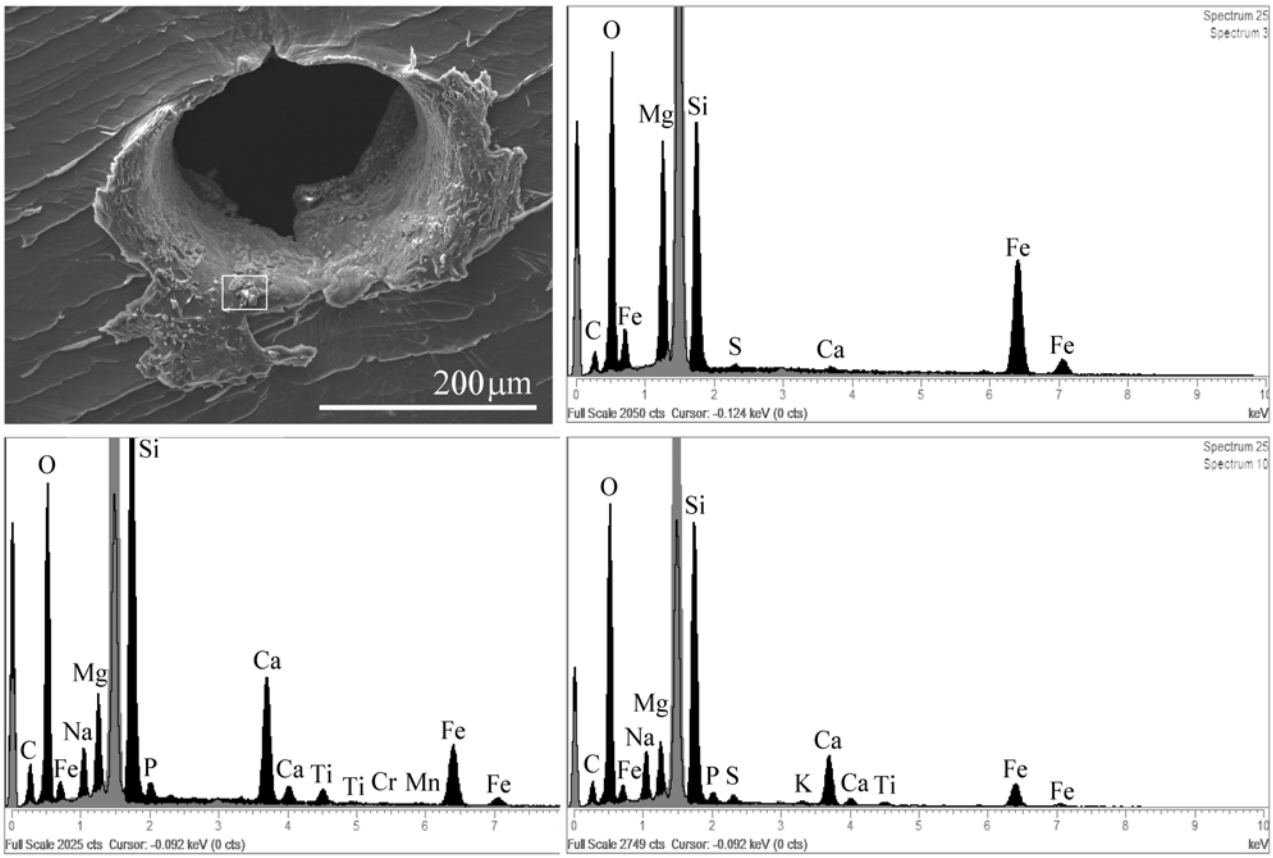

Fig. 10. C086W,1 SEI of crater, deformed by detachment from underlying frame, and ED X-ray spectra of three major residue components, all found in area of white box. Residue spectrum is in black; substrate is in gray.

analyses of 5 µm patches on the crater floor and wall (5 analyses in Table 2) is close to 3:2. When compared to residues from laboratory shots there is too little Mg to be from olivine, and too much for pyroxene. It could be an almost equal parts mixture of both, or glass/amorphous material, but more cannot be determined at the coarse (micrometer scale) spatial resolution of SEM-EDX alone. Auger imagery might reveal fine-scale heterogeneity. Reliable identification of any surviving minerals will require extraction of an ultrathin section for TEM analysis and electron diffraction study. For a rough estimation of the overall particle size and mass responsible for this feature, we have employed the relationship determined for single-impact bowl-shaped craters, although this may overestimate the particle mass if the particle were an aggregate with internal porosity. A bowl model would give a particle diameter of ~12 µm and mass of 3.2 ng. The structure, density, and probable porosity of this impactor is discussed further in the final section of the paper.

Stardust Foil C107W,1 (Fig. 13)

This foil shows a simple bowl-shaped crater of about 85 µm top lip diameter and an internal depth/diameter ratio of 0.58. Impactor residue is abundant in the floor and on the wall of the crater in patches up to 6 µm across, and appears to be compositionally homogeneous at the micrometer scale, comprising Mg silicate with minor Fe, Ca, Cr, Mn, and S. The thickest residues (assumed from low Al count rate) show a divalent ion to silicon ratio of almost exactly 3:2 (similar to that found in C091N,1). Identification of any mineral remnants will require FIB-TEM and electron diffraction analysis. From the SEM-EDX analyses, and from the depth/diameter ratio, we assume a particle density of ~3.2 g cm^{-3}, and hence use the crater top lip to particle diameter relationship to derive a particle diameter of ~17 µm and mass of 8.2 ng.

Stardust Foil C118N,1 (Fig. 14)

A simple, bowl-shaped, and fairly deep crater of ~68 µm top lip diameter is found on this foil, with an ambient plane depth/diameter ratio of 0.56. Residue is abundant as blocky fragments in patches up to 10 µm on the crater floor. From SEM-EDX analyses, the residue composition appears to be dominated by Na- and Ca-rich Mg silicate residue that does not seem to correspond to a stoichiometric mineral. Several small, discrete Fe- and S-rich grains were also seen. Several Ca-rich grains were found near the crater lip crest, along with small cupro-nickel grains.

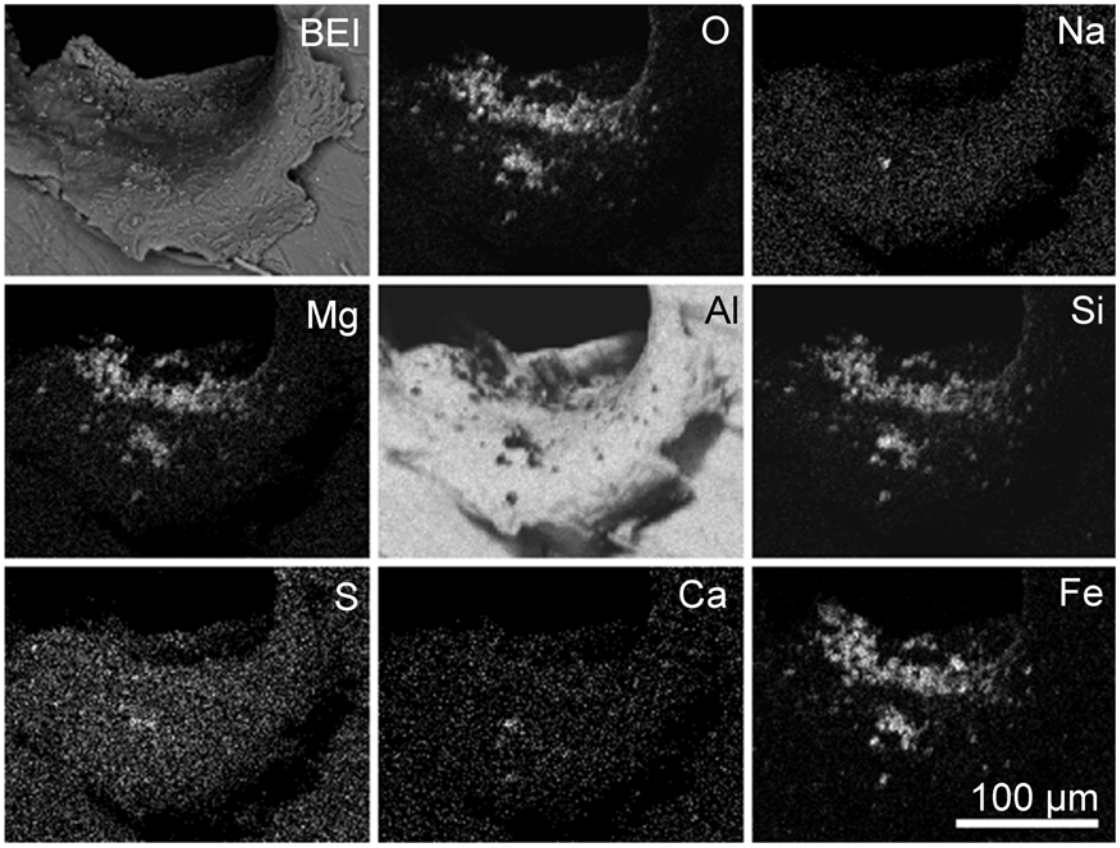

Fig. 11. C086W,1 BEI and X-ray maps of abundant residue in one part of the crater.

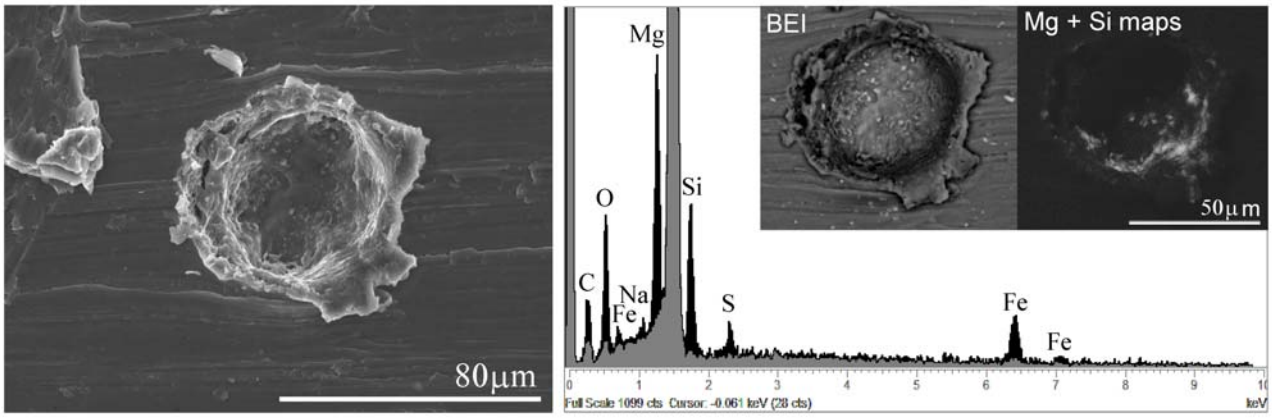

Fig. 12. C091N,1 SEI of crater; ED X-ray spectrum of a typical area of residue (spectrum is in black; substrate is in gray); BEI and Mg + Si X-ray map showing residue on crater floor and wall.

It is likely that these metallic grains are contaminants rather than impactor residue, as their composition is typical of artificial alloys. Subsequent nanometer resolution elemental mapping by Auger electron spectroscopy (Stadermann et al. 2007) has revealed that the relatively large interaction volume of our EDX analyses failed to resolve that there are at least two different sub-micrometer Mg Fe silicate materials in the residue at the crater lip, and that much of the Ca is also located in discrete sub-micrometer grains, associated with oxygen, but apparently no Si or C. The nature of the Ca-rich phase is unknown and will require FIB-TEM investigation. From the silicate residue composition and the depth/diameter ratio, we assume a particle density of ~3.2 g cm^{-3}, and hence use the crater top lip to particle diameter relationship to derive a particle diameter of ~14 µm and mass of 4.2 ng.

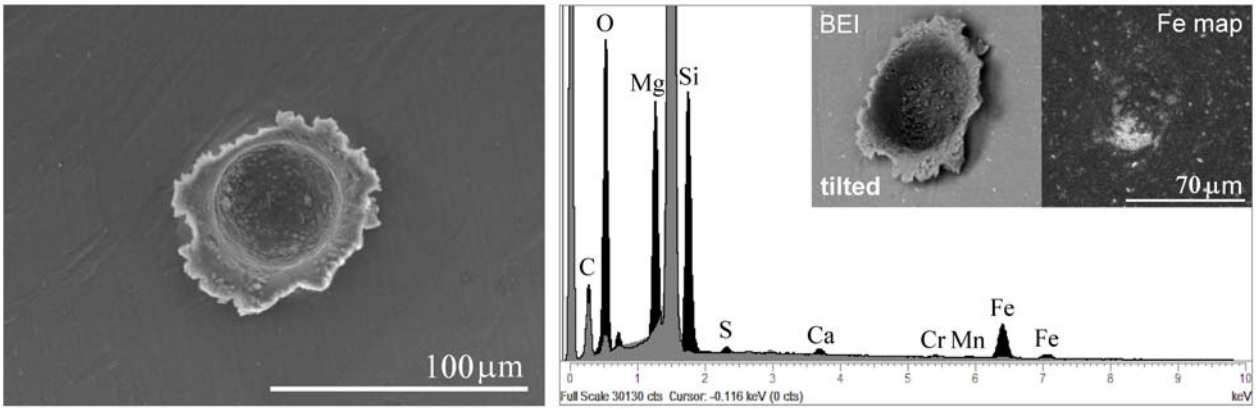

Fig. 13. SEI of crater on foil C107W,1; typical ED X-ray spectrum of residue (spectrum is in black; substrate is in gray), tilted BEI image, and Fe map to show distribution of coarse residue.

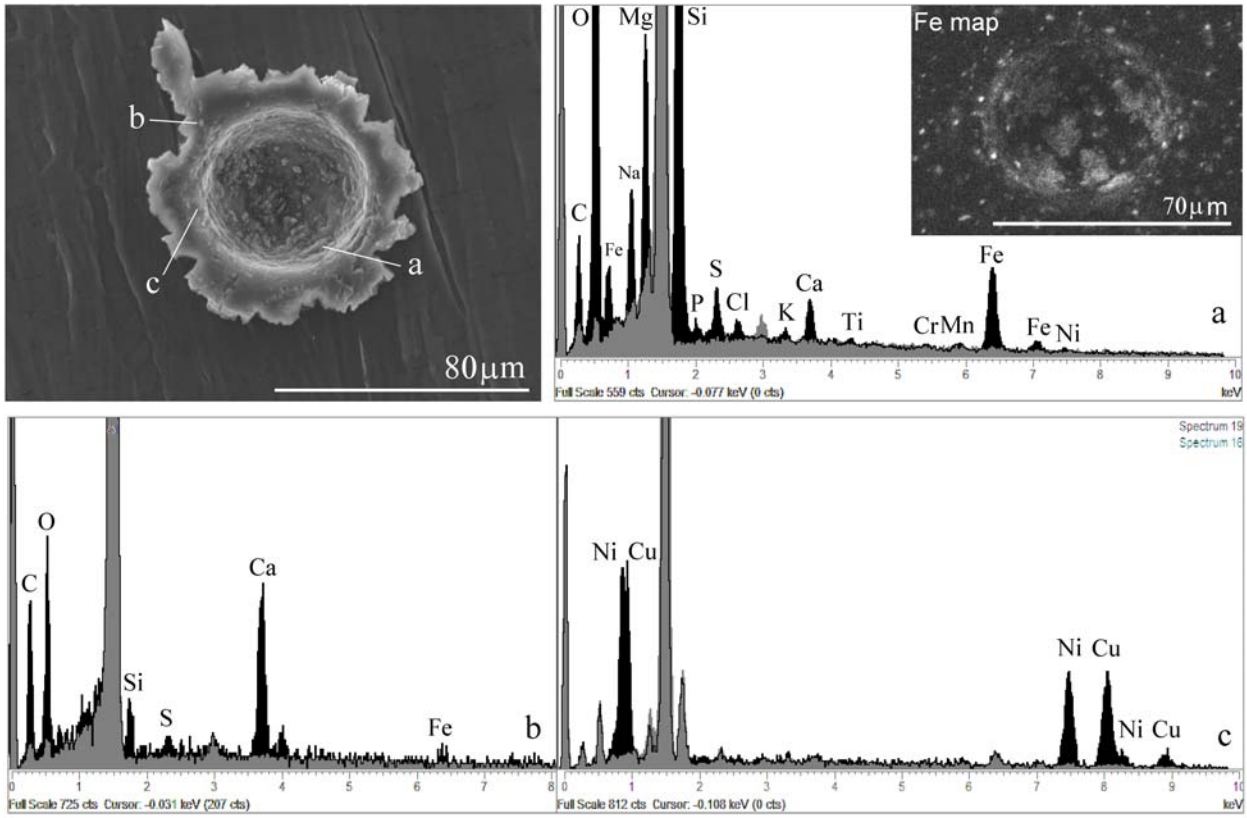

Fig.14. C118N,1 SEI and ED X-ray spectra of a) typical impact residue (inset Fe X-ray map shows distribution of coarse residue), (b) Ca-rich grain on crater rim, and (c) Cu- Ni-rich grain also on crater lip. Residue spectrum is in black; substrate is in gray.

Small Impact Features: Morphology and Residue Composition

Hörz et al. (2006) present a logarithmic total fluence plot for all crater diameter measurements conducted during the Stardust PE. Approximately 50% of all craters are smaller than 1 μm. If we accept our assumption that the experimental relationship of crater diameter to grain diameter (~4–5:1) is valid and that we can reliably measure a crater diameter from a poorly defined lip, this implies that Wild 2 dust is dominated by sub-micrometer grains, some of which are no bigger than a few tens of nanometers. Most of the very small craters (~95%) are found on just a few "clustered foils," and may be the result of a poorly understood disaggregation process prior to impact on the foil, as discussed by Westphal et al. (2008).

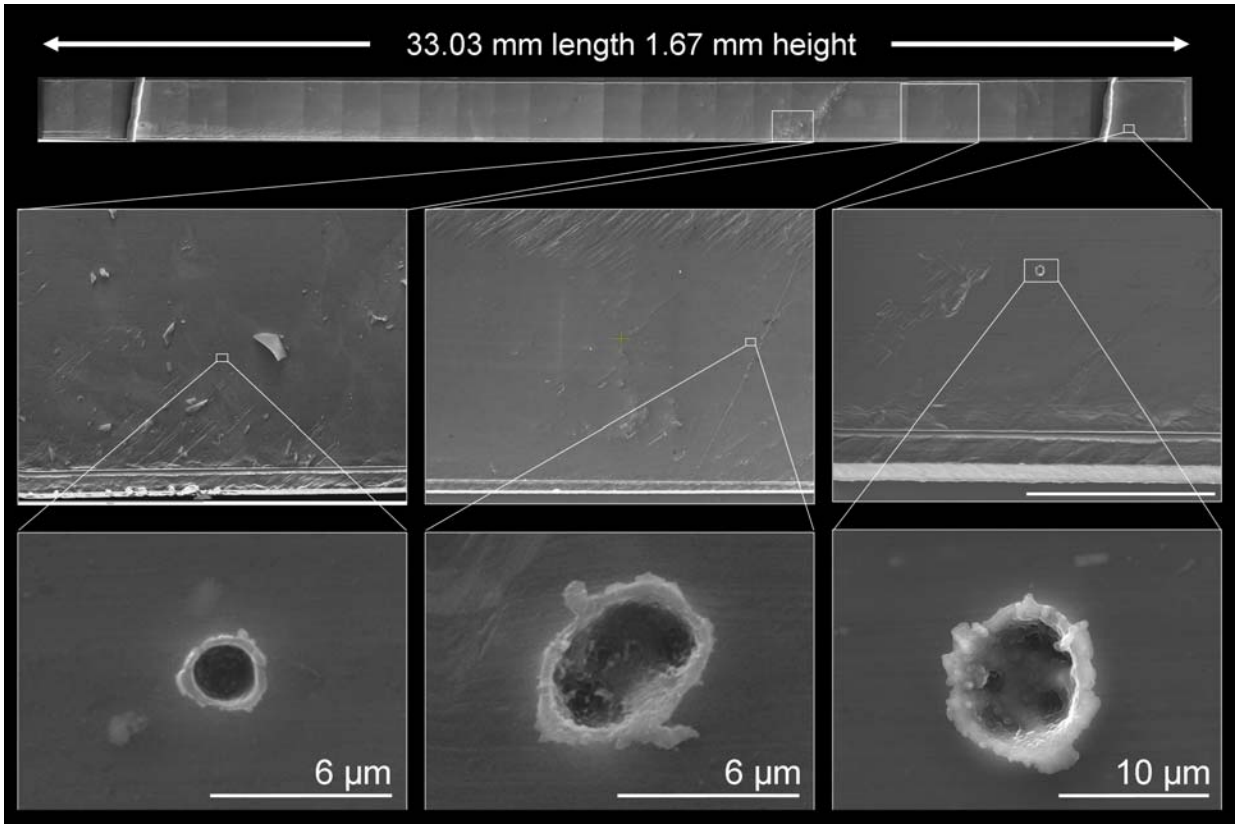

Fig. 15. SEI montage of a single whole foil (C125N,1) at low magnification, the location, and the detailed morphology of all the impact craters on that one foil (catalogued features 3, 4, and 2 from left to right, respectively).

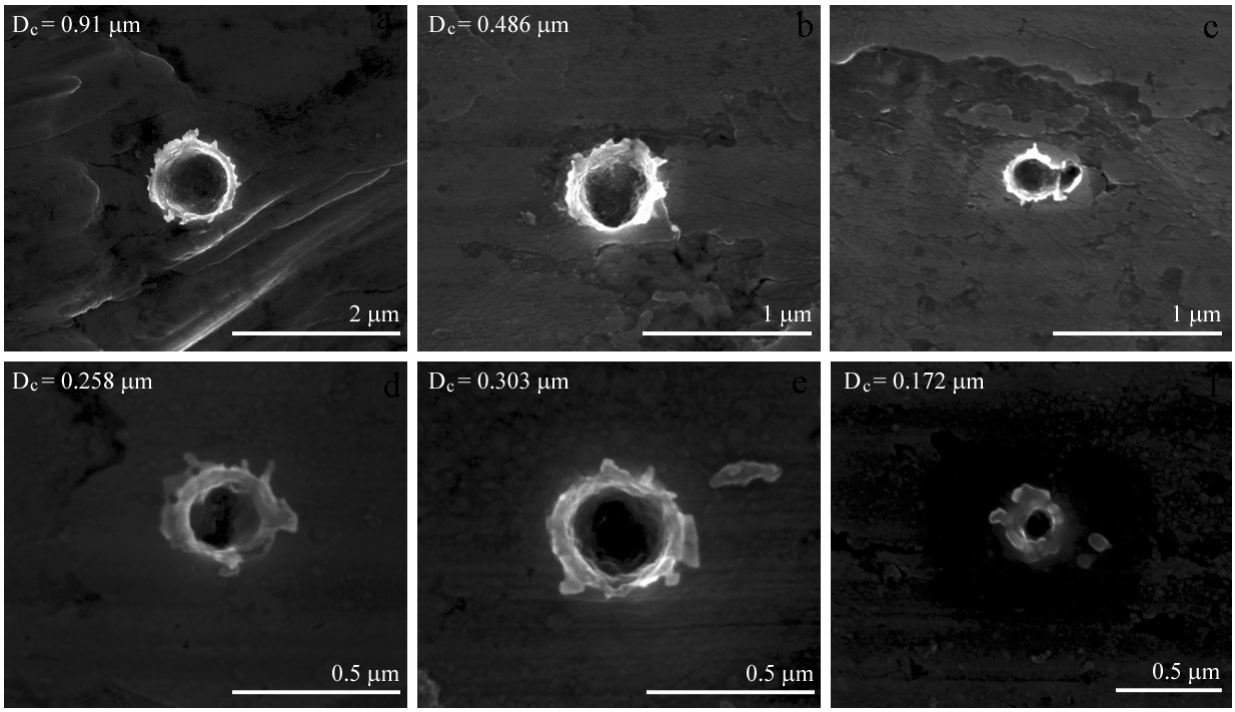

Fig. 16. SEI of typical small impact features on Stardust foil C100N,1: a) crater 1; b) crater 10; c) crater 11; d) crater 31; e) crater 19; f) crater 24.

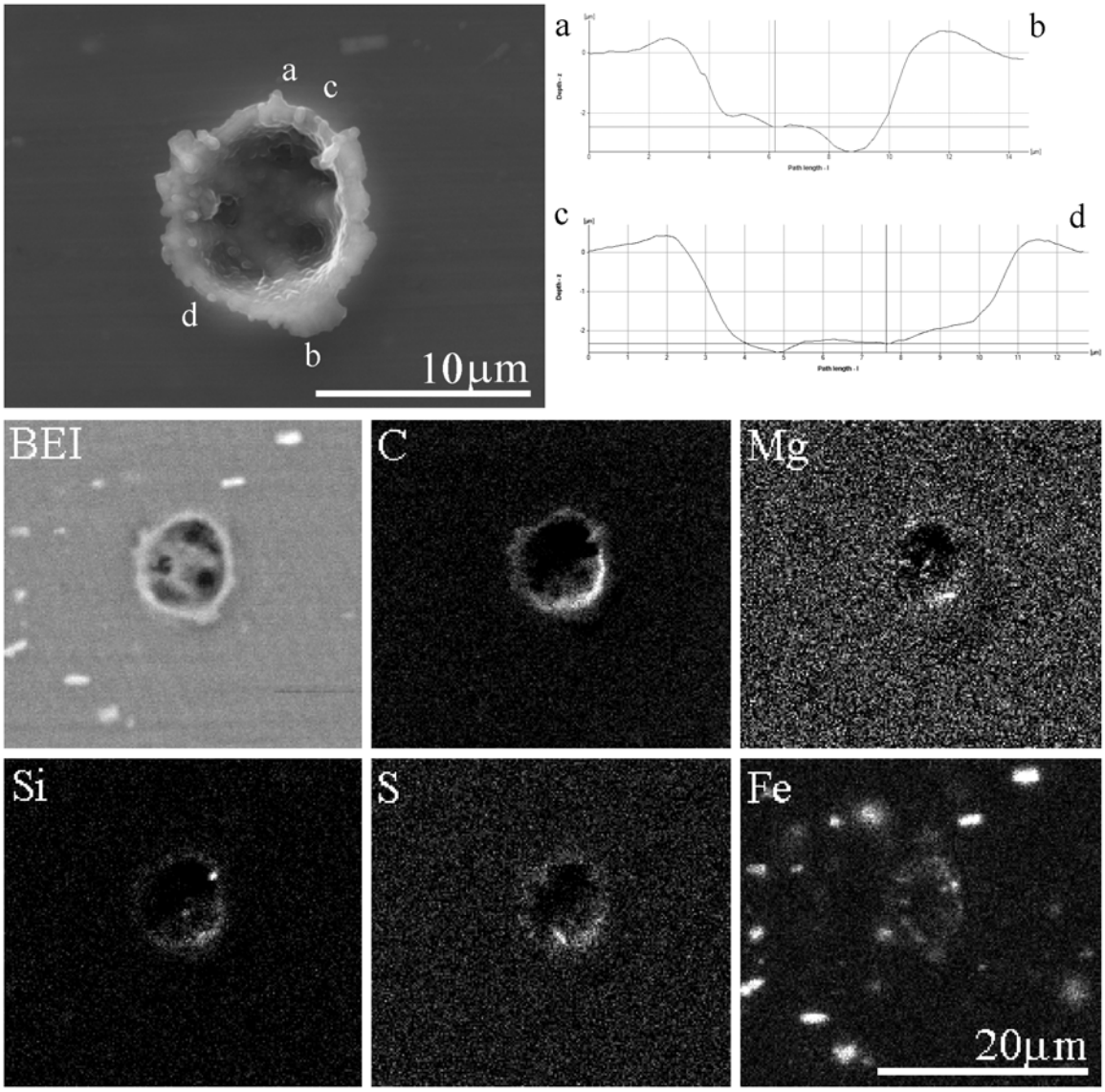

Fig. 17. SEI, depth profiles, BEI, and X-ray maps of impact feature 2 on foil C125N,1.

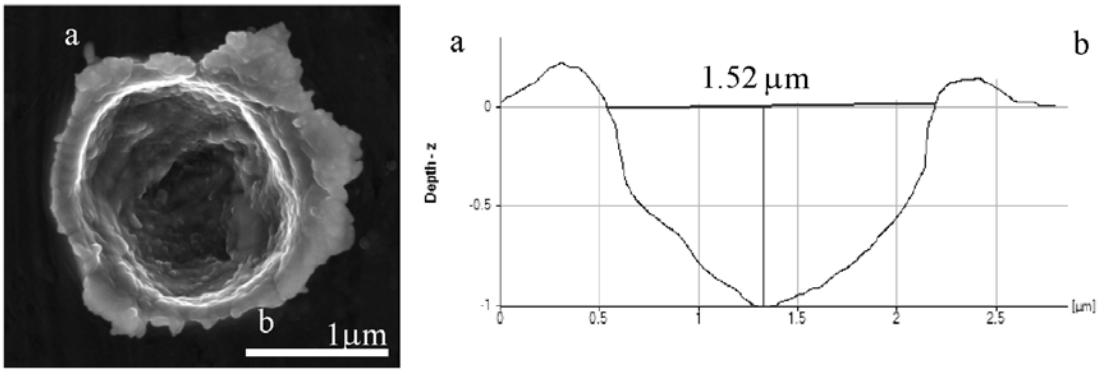

Fig. 18. SEI and depth profile of a micrometer-scale crater, foil C054W,1, feature 23, showing internal ambient plane diameter of 1.52 µm and depth of 948 nm.

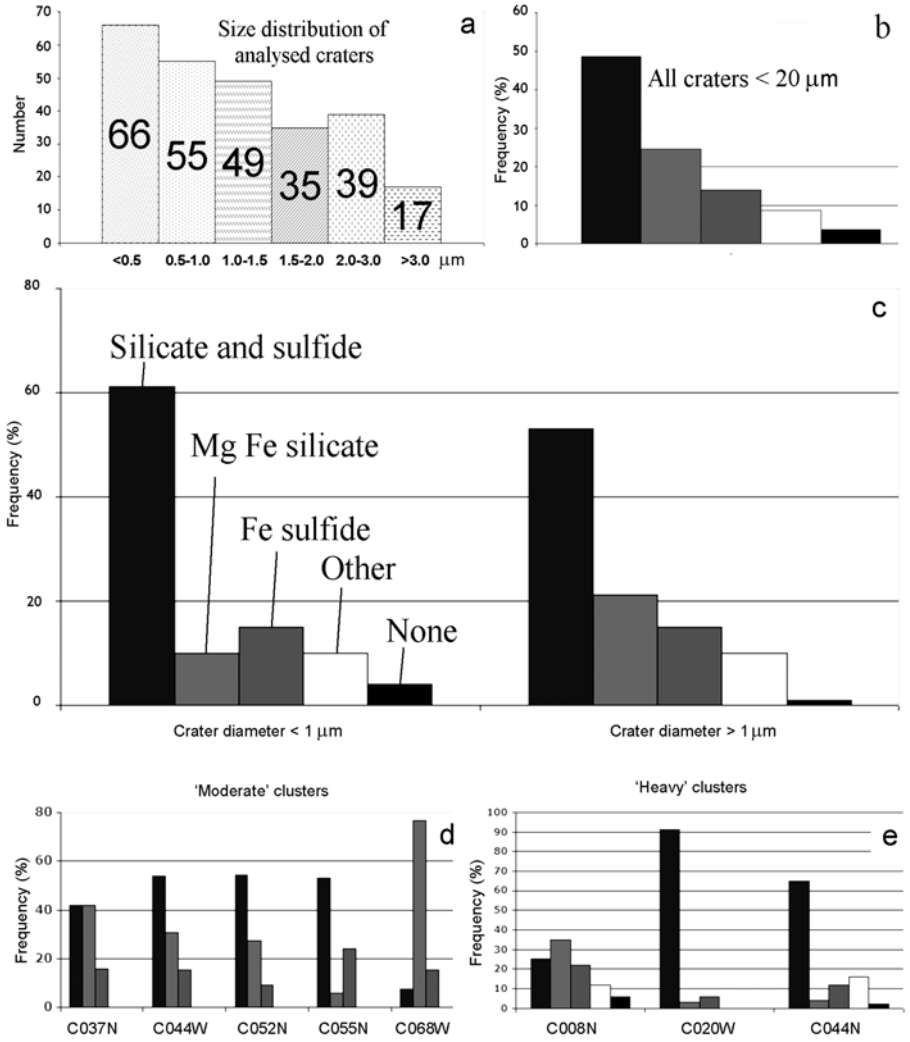

Fig. 19. a) Range of small crater sizes. b) Relative abundance of residue compositions. c) Comparison of residue composition abundance in sub-micrometer and micrometer-scale craters. d) Relative abundance of residue compositions in crater clusters on eight foils.

Figures 15 to 18 show typical examples of smaller Stardust foil craters. The shapes are very diverse, from simple circular bowl shapes to oval, irregular, and overlapped, with irregular depth profiles. Many craters show irregular internal distribution of melt and even discrete grains that Leroux et al. (2008) have shown may be crystalline remnants of the impactor. The numerous smaller craters (Fig. 19a) can be classified on major element compositional criteria from SEM-EDX (Fig. 19b). Spectra showing Mg and Si alone are defined as "Mg Fe silicate;" Fe (±Ni) and S alone defined as "Fe sulfide;" Mg, Fe, Si, and S together as "silicate and sulfide;" other element enrichments, e.g., Ca or Na, were defined as "other;" and the few cases (<5%) where no elemental signature above the Al foil substrate could be seen were classified as "none." Analyses were performed on 263 craters, all smaller than 5 μm. All the elemental signatures found are potentially extraterrestrial in origin; no artificial components were identified and thus there was no evidence of secondary ejecta from impacts elsewhere on the Stardust spacecraft. Nearly 50% of the impactors appear to have been composite particles containing variable amounts of Mg, Fe silicates (possibly olivines and/or pyroxenes) and Fe sulfides, while ~25% are Mg Fe silicates alone, and ~18% pure Fe sulfides alone (Fig. 19b). A few craters contain residues dominated by other elements such as Ca, and a small number apparently contain no residue that is distinguishable by EDX (Fig. 19b). A more careful study shows that the polymineralic nature of the residues is found at all scales down to 100 nm (Fig. 19c), although there may be a minor increase in the abundance of Mg, Fe silicate impacts in craters larger than 1 μm in diameter. Some foils have been impacted by numerous small grains (the clusters shown in Figs. 19d and 19e). Most clusters contain the typical range of residue compositions, although a few are dominated by a single composition (e.g., on foil C068W, Fig. 19d), and may have originated from

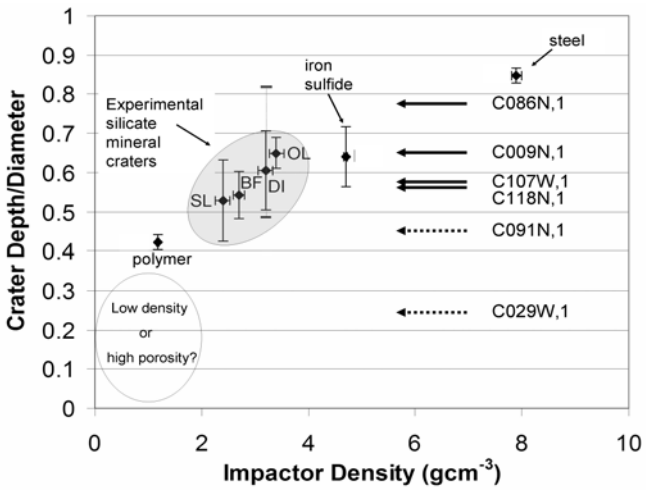

Fig. 20. Comparison of crater depth/diameter against particle density for a suite of experimental impacts at 6 km s^{-1} by polymer (polymethyl methacrylate), glass (soda lime SL), mineral (bytownite feldspar BF; diopside DI; olivine OL; pyrrhotite iron sulfide) and metal projectiles (steel). The average depth/diameter is plotted, with 1 standard deviation error bars. Note that the full range for 24 diopside craters (thin range bars) includes rare deep craters with depth/diameter that may exceed 0.8. A hypothetical field for low density/high porosity impactors is shown at bottom left. The depth/diameter values for six large Stardust craters are indicated at the right, with bowl shapes denoted by bold arrows, and compound features as dotted arrows. The deformed crater C086W,1 is not plotted as the true depth cannot be measured, although it is likely to have depth/diameter >0.5.

disruption of a single larger particle. For a discussion of possible mechanisms for cluster formation, see Westphal et al. (2008). A detailed survey of the residue composition and mineralogy of selected small craters has been performed using FIB-TEM as described in Leroux et al. (2008), confirming the preservation of olivine, pyroxene, and sulfide remnants.

INTERPRETATION OF CRATER MORPHOLOGY

The diversity of Stardust foil impact feature morphology is clearly apparent from the above descriptions, ranging from simple individual "bowl" shapes through irregular outlines to very complex, shallow, overlapped structures. Can we interpret dust particle structure and derive accurate particle dimensions, density, and mass from all Stardust craters by comparison with laboratory experiments?

Bowl-Shaped Larger Stardust Craters

From comparison to our previous experimental work, we suggest that the simple bowl-forms of C009N,1 C086N,1, C107N,1, and C118N,1 were each created by impacts of particles dominated by a single relatively dense mineral grain (e.g., Mg-rich olivine in C086N) or by a compact and dense aggregate. The relatively coarse residue in C086W,1 (probably a very large bowl form) also shows at least three different materials that may resemble the Fe-rich olivine and alkali-rich aluminosilicate assemblage seen in the matrix and chondrules of CR and CV chondritic meteorites. The presence of silicate residue with patches rich in S in C107N,1 and C118N,1 also suggests that even though most of their particle mass could have resided in a single coarse grain (albeit of unknown mineralogy), like most Wild 2 dust of 10 μm size, they are really polymineralic, and may have finer grained material adhering to the coarser components. A similar conclusion was reached by Flynn et al. (2006) from the compositional disparity between material found on the track walls and in the terminal particle of aerogel tracks. Coarse and fine-grained components do not have an opportunity to segregate in foil craters, although there is experimental evidence that finer-grained components can be damaged substantially during impact, and may therefore be more difficult to interpret, especially due to sulfur loss (Kearsley et al. 2007).

The depth/diameter ratio for craters C009N, C086N, C107N, and C118N also falls within the field defined by experimental data from non-porous silicate and sulfide projectiles (Fig. 20), and is clearly greater than that for polymer impacts (density ~1 g cm^{-3}). We conclude that the dust particles responsible for these craters were low in porosity, with overall grain density between 2 and 4 g cm^{-3}. However, the depth/diameter of C086N,1 is significantly greater than the average with standard deviation range for experimental silicate particles. Although morphology of our experimental craters from olivine and pyroxene is remarkably uniform, with few showing deviation from simple bowl shapes, even when the projectiles were known from SEM imagery to be inequant cleavage rhombs, the point of maximum depth is often slightly offset from the center of the crater as seen in plan view, and craters from a single mineral species may show a wide range of depth/diameter, which we attribute to irregular particle shape. Most fall close to the average depth/diameter, but occasional craters may be much deeper, as shown for the absolute range of diopside craters in Fig. 20. Previously, Burchell and Mackay (1998) have shown that perpendicular incidence of non-spherical projectiles can significantly change crater shape and the depth/diameter ratio. Accordingly, our new experiments have used very elongate calcium silicate projectiles with a maximum/minimum dimension ratio that may exceed 5. Their impacts show that such projectile shapes do influence crater shape, with wollastonite needles creating a wide range from elongate "boat-shaped" with the deepest point of the crater located toward one end, to very deep craters with a circular top lip (Fig. 21).

The positive correlation between crater circularity and depth/diameter for wollastonite powder shots indicates impact by grains presenting a range of aspects, from "belly-flop" by needles flying sideways (creating elongate,

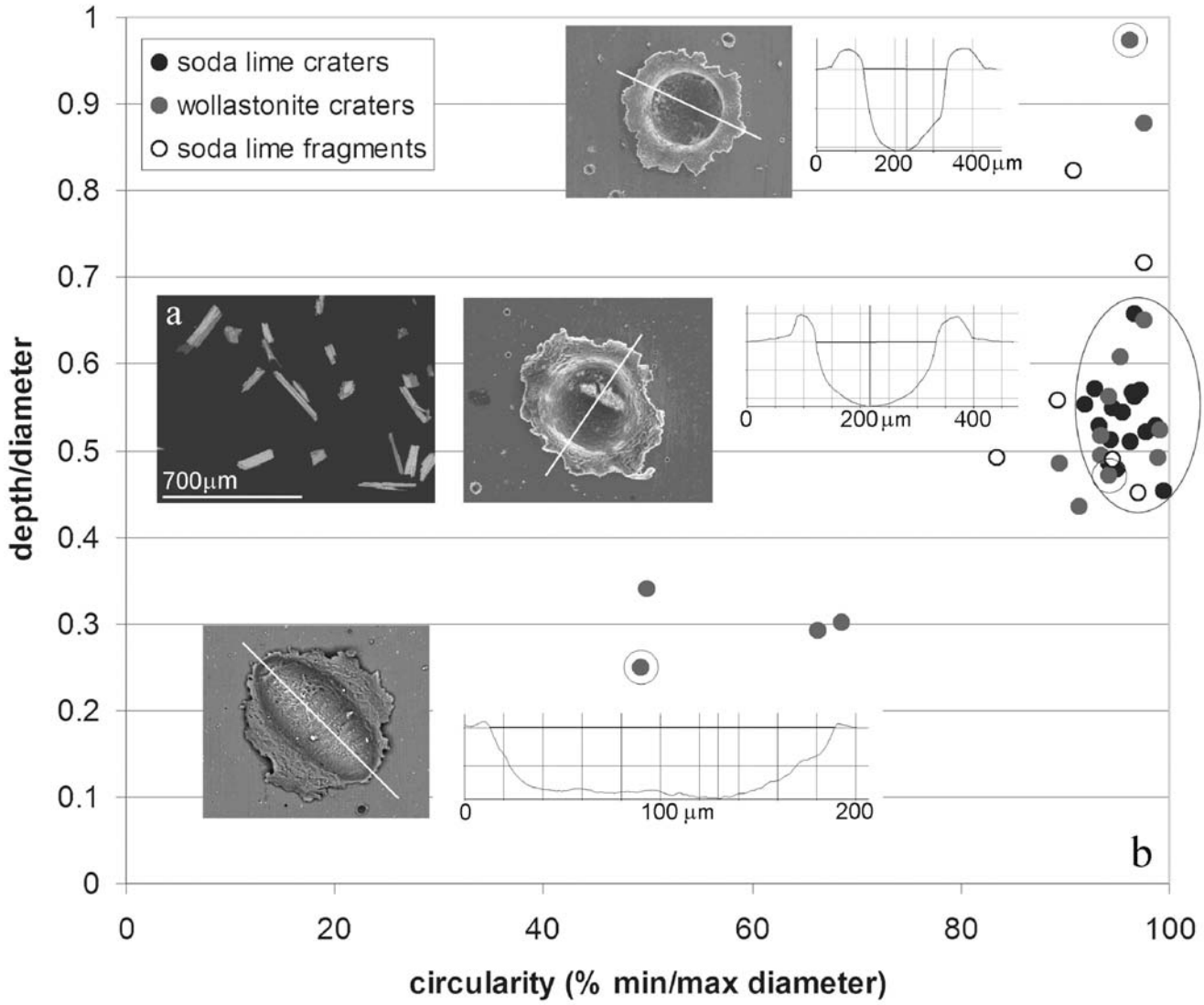

Fig. 21. Wollastonite experimental shot. a) BEI of typical projectiles superimposed on; b) background plot of depth/diameter versus circularity for craters from impacts by soda-lime glass (black and open rings) and wollastonite (grey), with superimposed illustrations of three wollastonite craters and their depth profiles along their long axis (marked by a white line). Craters produced by intact spherical soda-lime glass beads occupy the field of the oval ring). Illustrated examples are denoted by a ring around their plot position.

shallow craters) to "head-on" impacts that create narrow, deep craters akin to the process of rod-penetration by kinetic-energy anti-armor projectiles (e.g., Gee 2003). The dispersion of crater shape in soda-lime glass craters is also linked to small crater size, suggesting that a few monodispersive spherical beads had broken during the shot, creating irregular shards. We suggest that the high depth/diameter value for the circular Stardust crater C086N,1 is probably due to a "head-on" style of impact by an elongate cometary dust grain. The alternative hypothesis of a denser, more spherical shaped impactor can be rejected because all of the abundant residue in this crater is clearly from Mg-rich olivine, whose density is most unlikely to exceed 3.5 g cm^{-3}.

The morphology of many small craters and the features on C029W,1 and C091N,1 is more complex than that usually seen in most experimental craters, and probably reflects internal heterogeneity of mass-distribution in individual particles.

COMPLEX OVERLAPPED CRATER FIELDS (COMPOUND CRATERS) AND THEIR LABORATORY ANALOGUES

Is complex crater morphology a reflection of internal heterogeneity in the impacting particle? We believe the internal structure of almost all of our monomineralic experimental projectiles discussed thus far to be

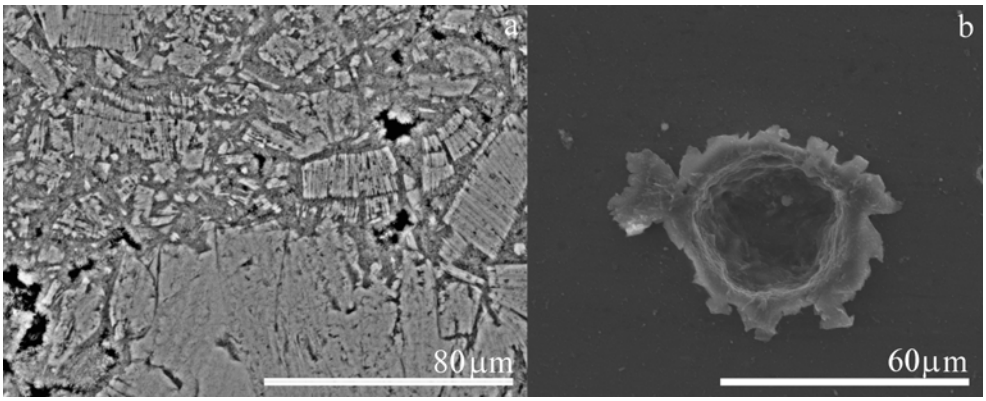

Fig. 22. Lizardite serpentine experimental shot. a) BEI of polished section reveals porosity (dark), internal heterogeneity of structure with platy crystals organized into stacked "vermicules" and fine cement, with occasional patches of talc. b) Complex crater formed by lizardite impact.

homogeneous and lacking substantial porosity, although the mineral grains will have planes of weakness controlled by the crystal lattice. Our experimental shots with three types of porous projectiles (powdered lizardite, Allende meteorite powder, and artificial silicate and sulfide aggregate particles) have yielded useful analogues that help us to understand the range of crater shape complexity.

Impacts by relatively weak monomineralic samples, e.g., lizardite with a complex internal platelet structure and with porosity of about 5% by volume (Fig. 22a), yield crater morphology that is usually a radially symmetric bowl, although more complex crater forms may occasionally be generated (Fig. 22b).

Polymineralic impactors, such as the crushed Allende carbonaceous chondrite meteorite powder responsible for the crater illustrated by Hörz et al. (2006), may yield apparently circular craters of similar depth to monomineralic impactors, but with more complex sub-surface morphology, only fully revealed by a detailed digital elevation model. Porosity measurements for Allende cluster around 20%, but with a range between 10 and 30% (Britt and Consolmagno 1996), and sections of Allende clearly show that a powder will yield particles with great internal heterogeneity in composition and component grain size. The wide range of internal composition includes olivines of diverse Fe:Mg ratios, pyroxenes both Ca-rich and poor, feldpathic glass, iron-rich oxides, metal, and sulfides. Wide variation also occurs in individual component size, micrometer-scale olivines forming matrix, to sub-millimeter intergrowths of olivine, pyroxene and glass in chondrule fragments. A grain made of this mixture might result in much more complex interaction with the Al substrate, and may be considered as a suite of almost synchronous and near-superimposed impacts by each of the individual grain components. As a result, the crater excavation flows from each component do not complete movement before nearby arrival of the next subgrain, whose impact therefore creates interference in crater morphology. Well-defined uplifted and overturned crater rims, so typical of single mineral impacts may not be developed between all the component features inside the main feature, although the composite impact structure may be surrounded by an external rim.

However, although both of the above experimental analogues generate craters that are more complex than simple smooth bowl shapes, they are still relatively compact and deep features. Neither of these projectile types creates structures that closely resemble the most complex broad, shallow, and overlapped compound features found on Stardust foils such as C029W,1.

Several authors have attempted creation of overlapped craters by experimental simulations of clustered grain impacts. Schultz and Gault (1985) produced multiple impacts by a cloud of closely spaced particles onto granular and porous media using forward-directed ejecta from a metallic foil suspended above the final target. However, due to the spacing between primary and secondary targets, the separation of the resulting individual fragments was greater than the individual particle diameters, The effect is thus to disperse impact points, and their resulting overlapped craters show very complex shapes, difficult to compare to Stardust features due to the very large number and broad spread of features, and the different behavior of the granular target materials. Hörz et al. (1994, 1998) used shots of soda-lime glass projectiles onto 4 μm Al foil suspended over a metal witness plate to generate clouds of small particles. The damage patterns created by their tightly clustered debris clouds (with little separation between foil and witness plate) show similarities to the complex Stardust craters, but are more regular and symmetric in structure, probably reflecting the relatively simple structure of the debris cloud from a spherical primary projectile when compared to the wide range of subgrain sizes that may be present in cometary dust aggregates (10 nanometers to 100 μm).

As an unintended by-product of our shots of steel spheres onto experimental Al foil targets, we have observed overlapped crater fields created by ejecta from oblique

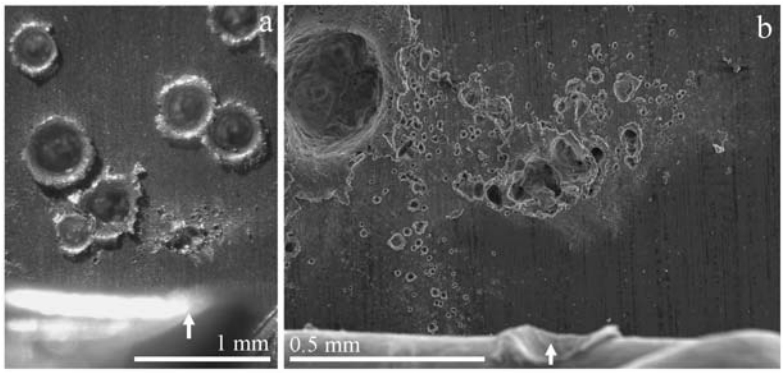

Fig. 23. a). Optical micrograph of Stardust foil light-gas gun shot target impacted by stainless steel spheres. Arrows show location of oblique/ grazing impacts on the edge of the foil target, producing a conical ejecta cone that impacted as densely clustered particles on the Al supporting plate beneath. b) SEI of impact features created by near-synchronous impact of an ejecta cloud from the oblique impact in (a).

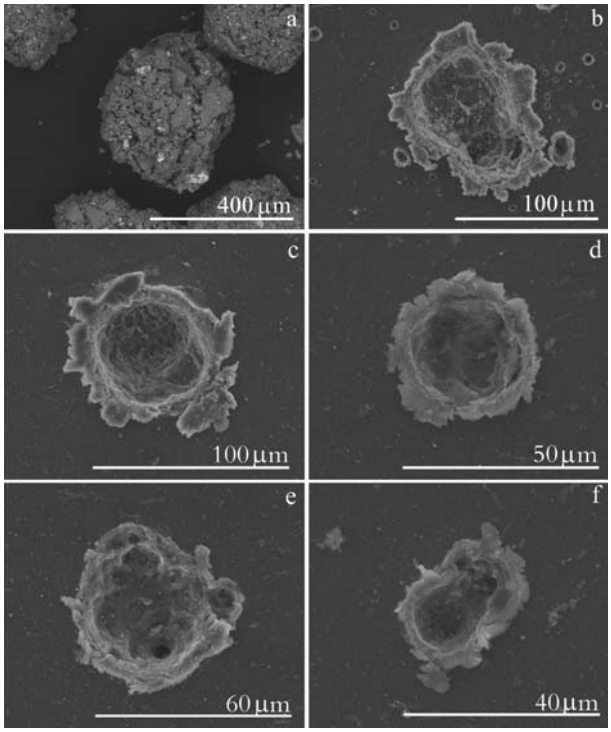

Fig. 24. a) BEI of an artificial aggregate projectile, produced by aerosol droplet impregnation of silicate and sulfide mineral powder, note the very high porosity (and hence presumably relatively low density); b) SEI of complex impact feature from artificial aggregate impact, the large depression to upper left contains olivine residue, that to lower right contains Ca-rich clinopyroxene and olivine residue. c–f) secondary electron images of experimental aggregate impact craters on a thick Al-alloy target.

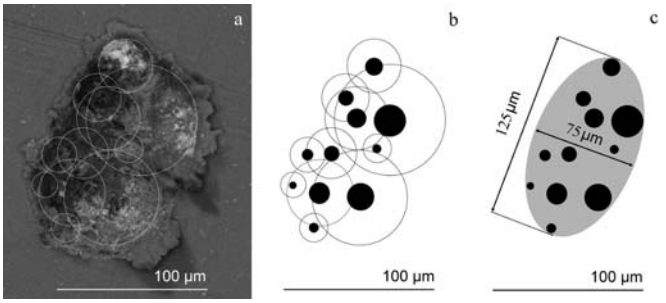

Fig. 25. a) Model of overlapping circular crater forms fitted to the outline of C029W,1. b) Impacting particle outlines showing spatial distribution. c) Superimposed overall particle outline.

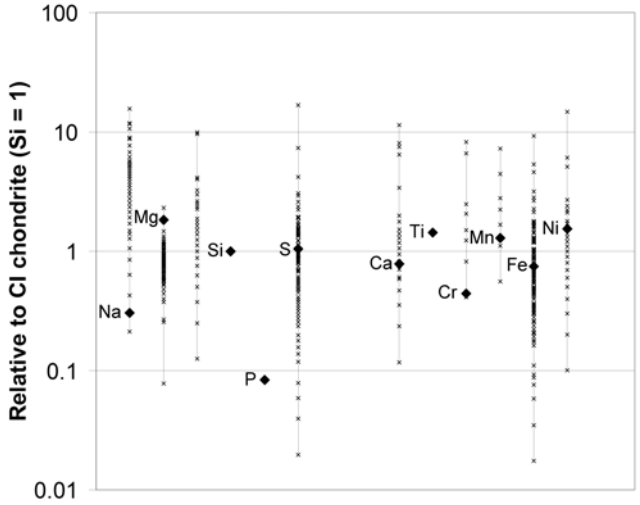

Fig. 26. Bulk composition of residue in C029W,1 (bold diamonds) compared to individual IDPs (joined crosses; from Table 38 of Rietmeijer 1998), both normalized to CI chondrites (Lodders 2003). Logarithmic plot; elements normalized to Si = 1.

impacts onto the inclined edge of the wrapped foil (Fig. 23). These closely resemble some of the Stardust foil impact features, although they also show wider dispersion of minor "satellite" craters as well as concentration into a larger compound structure.

However, we do not suggest that the overlapped compound Stardust features are the result of ejecta clouds derived from the Stardust spacecraft (but see Westphal et al. 2008), nor that they indicate closely clustered yet separate particles. Instead, we suggest that their complex shape indicates impact by an irregularly organized cluster of grains, held together loosely in a porous aggregate.

Although the strength of subgrain cohesion is unlikely to play a major role in crater development due to impact by cometary dust, it is a serious limitation in realistic laboratory simulation, as it causes the majority of aggregate projectiles to disintegrate before reaching the target. Nevertheless, our recent experiments (Fig. 24) show that the problem is not insuperable, and our first shots of artificial aggregates have yielded compound craters with depth/diameter values as low as 0.27–0.35 (Fig. 24e).

As the mechanical strength of the material binding the particle internal subcomponents may play little part in the actual impact process (beyond restricting the spatial separation), it may appear difficult to distinguish impact features created by a loosely bound aggregate of small particles held together by grain surface interlocking, sintering, or a binding material of low density such as ice or organic matter (e.g., the polymer bound aggregate craters of Fig. 24) from those of a cloud of small particles that are not physically attached but are closely associated spatially (and therefore temporally) e.g., the ejecta cloud in Fig. 23.

However, the degree of "clustering" may provide an important criterion, in that experimental impacts by particle clouds usually show numerous minor satellite craters, decreasing in number with distance away from the central concentration of impact features (e.g., Fig. 23). We suggest that a lack of such satellite craters may be a reliable criterion from which to recognize true aggregate impacts.

The internal structure of impact features such as the compound structure on foil C029W,1 and feature 2 on C125N,1 suggests that they were probably formed by synchronous impacts of numerous closely spaced centers of mass, causing mutual interference of crater bowl excavation flow fields. The result was a relatively broad and shallow structure with an irregular external overturned lip and internal uplifted septa between bowl shapes. The lack of any cluster of nearby impact structures and the evidence for very closely spaced yet synchronous minor impacts in a tightly defined area strongly suggests that this is an impact by a single porous aggregate particle, rather than fortuitous coincidental impact within a small area by separate grains. Although it is not possible to generate an indisputable model for the mass distribution within such an impactor from the resulting complex impact feature, it is useful to examine the simplest scenario (Fig. 25).

In the case of a feature such as C029W,1, reconstruction of the impacting particle locations and dimensions is made difficult by the complexity of the fine structure. The oval regions dominated by sulfide (Fig. 8e) and Ca-rich silicate (Fig. 8c) each show a bowl-shaped profile (Fig. 5), albeit laterally deformed, suggesting that they may have been formed by relatively dense subgrains. We have estimated their original crater diameter (and hence particle diameter and mass) by finding the best fit of a circle to the top lip of the remaining, undisturbed external circular profile (see Fig. 25). A similar approach has been taken for other depressions whose depth profile is close to a simple bowl. For features toward the center, the true crater diameter may be greater than our estimation as the synchronous excavation of neighboring features has removed any well-defined crater top lip, leaving a more irregular septum, whose apex probably represents a lower portion of the crater wall.

The broadest and very shallow part of the feature (lower right of Fig. 25a) has a much more irregular floor that does not show simple bowl forms. Together with the finely disseminated residue in this area, this may suggest that this part of the aggregate was a very porous, fine-grained mixture, possibly amorphous silicate and sulfide. The overall composition of the integrated crater residues (extracted from EDX maps of the crater area) also shows that the particle responsible for the feature on C029W,1 had major element proportions similar to chondritic aggregate and cluster interplanetary dust particles (IDPs) and carbonaceous chondrites (Fig. 26). Both SEM EDX and TOF-SIMS found abundant carbon associated with the rim of this feature, probably organic matter.

Table 3. Suggested subgrain components responsible for feature on C029W,1. Subgrain diameters are based on the density-corrected crater top-lip diameter relationship of Kearsley et al. (2007). The aggregate volume is based upon the area of the oval reconstruction in Fig. 25c and an assumed thickness calculated from the minimum subgrain diameter (3.4 mm). Aggregate density is calculated from the oval disk volume and the subgrain total mass, and porosity is calculated from the proportion of the oval disk volume not occupied by the subgrain volumes shown above.

Feature	Diameter (μm)	Density (gcm^{-3})	Subgrain diameter (μm)	Volume (μm^3)	Subgrain mass (μg)	Comp.
1	74	3.3	14.8	1697	5.4	Pyroxene?
2	63	<3.2 (2.4?)	17.5	2806	6.8	Mixed
3	45	3.2	9.0	382	1.8	Mixed
4	42	3.2	8.4	310	1.0	Mixed
5	36	4.6	7.2	195	0.6	Fe Ni S
6	34	3.2	6.8	164	0.5	Mixed
7	32	3.2	6.4	137	0.4	Mixed
8	24	3.2	4.8	58	0.2	Mixed
9	19	3.2	3.8	29	0.1	Mixed
10	19	3.2	3.8	29	0.1	Mixed
11	17	3.2	3.4	21	0.1	Mixed
Total				5829	19	
Aggregate	125 × 70	0.79		23,553	19	C chond.?

Although it is not possible to derive an accurate mass distribution model for the broad feature, in order to make a "maximum particle mass" model for assessment of overall aggregate density and porosity, we used a particle size and mass estimate based on a small dense grain with the same crater diameter to particle diameter relationship as dense silicates (Table 3). This will almost certainly overestimate the mass contribution from this component of the aggregate, will cause overestimation of overall crater MgO relative to SiO_2 wt% (apparent if such analyses are compared to the bulk composition given in Table 1), elevate the calculated aggregate mass and the inferred aggregate density, and depress estimated porosity. The simplest model must also assume impact of an aggregate that is essentially two-dimensional (i.e., all the mass centers lie on a plane perpendicular to the direction of impact. The superposition of some bowl shapes on larger features suggests that this model is incorrect, with a sequence (albeit near-synchronous) of small impacts, implying a third dimension in the impacting particle. However, we have no way to measure "thickness" along the axis of impact, and our model of the overall aggregate size (Fig. 25c) therefore shows the projection of mass centers in two dimensions, with an oval outline for the whole structure. The shortcomings of such a physical model are also immediately apparent in the diagram of mass-center distribution in Fig. 25b. The separation of aggregate components provides no mechanism to hold the particles together, and strongly suggests that much of the aggregate was probably a fine-grained matrix. How was this particle held together? There is no need to invoke great strength for the aggregate; if the very finest grained components were of markedly inequant shape, they may have formed a mechanically interlocking matrix, as is often found in porous terrestrial sediments with irregular grain shapes (e.g., Rutledge et al. 1995). The presence of mixed fine-grained Mg-rich silicate and Fe sulfide residue throughout the entire impact feature suggests that this type of material may have coated the larger subgrain components. The presence of carbon-rich areas in C029W,1 and the complex crater of C125N,1 also suggests that organic material was present, and may have acted as a binding agent.

The calculation of Table 3 shows that even the "highest-mass" model for the aggregate particle responsible for C029W,1 implies a very high internal porosity (75%) and low overall density of 0.79 g cm^{-3}. This is very similar to the estimation of density (0.8 g cm^{-3}) that one might obtain from plotting the average depth/diameter ratio of 0.24 into the centre of the hypothetical low density/high porosity field extrapolated onto Fig. 20.

For the "flat-bottomed" impact feature on C091N,1, it is even more difficult to estimate the size and mass of the grain aggregate components as their impacts appear to have been so close together that it is not possible to measure the size of individual features within the overall impact feature. A model of porosity for this aggregate particle can therefore only be obtained from assumption of the overall grain density from the depth/diameter ratio. The scatter on experimental data in Fig. 20 shows this density estimation to have relatively poor precision, with likely the likely value lying between 1.8 and 2.6 g cm^{-3}. With a probable solid mafic silicate grain density of ~3.2 g cm^{-3}, this would imply internal grain porosity between 20 and 45%. A depth profile of the artificial aggregate crater illustrated in Fig. 24d shows a similar "flat-bottom" to that in C091N,1, albeit with an even shallower depth/diameter value (0.32 versus 0.45, respectively).

IMPLICATIONS FOR THE STRUCTURE AND COMPOSITION OF WILD 2 DUST GRAINS

The comparison of crater size, morphology, and residue composition to that seen in laboratory impacts clearly shows that some Stardust foil impacts were produced by large (10 to 60 μm in diameter) grains of dense (~3 g cm^{-3}) silicates dominated by single olivine grains, or low-porosity aggregates of olivine, pyroxene, and sulfides. These impacts created relatively simple, bowl-shaped craters, and are probably equivalent to the large particles found at the terminus of "carrot-shaped" aerogel tracks. However, there is also abundant evidence from residue heterogeneity in bowl-shaped craters that the main mass was accompanied by finer grains of diverse silicate and sulfide composition, perhaps together resembling the particle reported from track 57 ("Febo"), shown as Fig. 2 of Brownlee et al. (2006). Such material may usually be stripped from the surface of a larger grain during emplacement in aerogel. Larger features also include compound craters produced by impacts of porous, low-density aggregates of complex shape and diverse composition, whose integrated bulk composition may approach that of CI carbonaceous chondrites for refractory major elements, and whose Mg/Si, Fe/Si, and S/Si atomic ratios fall within the range shown for aggregate IDP shown by Rietmeijer (1998). Some of the micrometer-scale components in these large (100 μm scale) aggregates were apparently made of even smaller grains (tens of nanometers). The diverse shapes of the myriad smaller impact craters and their range of preserved residue compositions also suggest that they may have been formed by these same sub-micrometer grains (albeit smaller aggregates), and the association of multiple mineral components has been confirmed in FIB-TEM studies (Leroux et al. 2008). Together, this aggregation on scales from a few nanometers to tens of micrometers probably corresponds to that seen in numerous electron microscope studies of chondritic porous (CP) IDPs, e.g., Fig. 1 of Bradley (2003), the cluster and aggregate IDP discussed at length by Rietmeijer (1998), and may be akin to the structures inferred from spectroscopic remote sensing of dust (e.g., Greenberg and Gustafson 1981). As it is suspected that porous aggregates break up on entering aerogel to form the "bulbous" tracks described by Hörz et al. (2006), it seems that Al foil impacts provide the best record of the abundance and size of fine dust aggregates from comet Wild 2.

In situ analyses by EDX are clearly valuable for the recognition of interesting impact residues, and can sometimes provide sufficient quality to determine major-element concentrations in parts of coarser residues, and hence assess whether they are likely to be derived from stoichiometric mineral materials. However, the interaction volume from which X-ray information is obtained is greater than the size of the smaller grains that accompany the coarse particles, and which comprise the bulk of the aggregate particles across their entire size range from tens of nanometers to 100 μm. Similarly, where EDX suggests a non-stoichiometric bulk composition for a larger grain, it may be integrating data from an intimate aggregate of stoichiometric phases. It will therefore be necessary to use higher resolution techniques such as Auger spectroscopy for surface characterization of sub-micrometer elemental assemblages and FIB-TEM for more precise mineralogical identification. Both analytical approaches require intense future research effort on the Stardust crater residues described in this paper. Further laboratory experiments are also necessary to yield a better understanding of the artefacts generated by impact processes and how these might influence our interpretation of Wild 2 dust composition.

In particular, there is no current experimental simulation of impact by porous, low-density aggregates of extremely fine-grained mineral and amorphous materials that we could use to predict the behavior of glass with embedded metal and sulfides (GEMS) particles on encountering Al foil at 6.1 km s^{-1}. Although there is still debate as to whether the presence of GEMS may indicate pristine, unaltered material from the pre-solar interstellar medium (Bradley 1994; numerous other papers), unequilibrated material from an inner Solar System origin (Davoisnes et al. 2006), or both (Messenger et al. 2003; Keller and Messenger 2006), they are an important structure to seek in the Stardust collection. GEMS may be extremely difficult to recognize in aerogel tracks, due to the creation of similar-looking material by mixing of impacting dust with the aerogel (Chi et al. 2007). Unfortunately, we do not yet know how to recognize the products of impact by GEMS (and other amorphous materials) on foil. For these reasons, our present study cannot yet give an estimation of the relative abundance of stoichiometric and amorphous grains in the finer grained portion of the dust population. This is a major shortcoming, as it denies us the use of a potentially valuable criterion with which to assess the contribution of fine-grained, poorly crystalline material to Wild 2 dust, and hence determine how much real Stardust (as opposed to inner Solar System crystalline silicate) is present. In the future, residue surface texture may yield important information as to particle fine structure, and is probably worthy of detailed study. Our laboratory experiments suggest that the fine (micrometer-scale) surface texture of the crater interior also varies, with irregular but relatively smooth sheets of residue from amorphous material such as glass (soda-lime or basalt) and polymer impactors, in contrast to blocky fragments of mineral impactors.

SUMMARY AND CONCLUSIONS

SEM-EDX, routinely used as an investigation technique in surveys of impact craters on metallic targets, appears to be a very useful and sensitive way to obtain statistical surveys of

Wild 2 dust. It permits rapid location of impact features, allows measurement of their size and three-dimensional shape, and recognizes major-element chemistry in their residues. It is particularly well-suited to preliminary characterization of the smallest size fraction, by far the most numerous grains, but which are very difficult to examine when trapped in aerogel. In future studies, SEM-EDX (along with TOF-SIMS) should be considered as one of the first survey and analytical tools in a sequence of analysis protocols to locate compositionally rare and interesting particles, to then be followed by high-resolution elemental and isotopic techniques such as Auger spectroscopy, FIB-SEM, FIB-TEM, and NanoSIMS.

SEM studies of craters on Stardust Al foil have shown evidence of impact by particles of a wide range of size, from a few tens of nanometers to nearly 60 μm in diameter. Many of the large impact features (>20 μm in diameter) were made by dense silicate grains, some dominated by a stoichiometric mineral of homogeneous composition, accompanied by smaller quantities of diverse silicate and sulfide composition. In addition, several large craters show evidence for impact by low-density porous impactors that were assemblages of micrometer-scale higher-density grains, held together by a very fine-grained matrix material, possibly carbon-rich. The very numerous smaller craters (<20 μm in diameter) were created by impacts of single silicate or sulfide grains of a few tens of nanometers to a micrometer in diameter, or by aggregate particles, probably of low overall density and containing a mixture of nanometer-scale silicate and sulfide components. We conclude that the large numbers of easily accessible cometary dust samples preserved in Stardust Al foil craters constitute a valuable resource for future research.

Acknowledgments—We thank NASA for allowing us access to Stardust Al foils, and for the supply of flight spare foil for our laboratory experiments; the Natural History Museum London for access to electron microscope facilities (A. T. K. and P. J. W.); PPARC for support of the work by M. J. B. and M. J. C. on the light-gas gun at the University of Kent, Canterbury (M. J. B. and M. J. C.); the Centre National des Etudes Spatiales for financial support (J. B. and H. L.); the Deutsche Forschungsgemeinschaft for grant STE 576/17-1 (T. S.); and NASA for grant NNG05GJ26G (F. J. S.) J. P. B. acknowledges support by NASA's cosmochemistry (grant no. NAG5-10696), SRLIDAP (NNH04AB49I), and Stardust Participating Guest programs (grant no. NNH06AD67I). This work was performed in part under the auspices of the U.S. Department of Energy, National Nuclear Security Administration by the University of California, Lawrence Livermore National Laboratory under contract no. W-7405-Eng-48. Review and suggestions for revision by Gero Kurat and Mike Zolensky are gratefully acknowledged.

Editorial Handling—Dr. Christian Koeberl

REFERENCES

Bernhard R. P. and Hörz F. 1995. Craters in aluminum 1100 by soda-lime glass spheres at velocities 1–7 km/s. *International Journal of Impact Engineering* 17:69–80.

Bernhard R. P., Durin C., and Zolensky M. E. 1994a. Scanning electron microscope/ energy dispersive X-ray analysis of impact residues in LDEF tray clamps. In *LDEF— 69 months in space*, vol. 2, edited by Levine A. S. Washington, D.C.: National Aeronautics and Space Administration. pp. 541–549.

Bernhard R. P., See T. H., and Hörz F. 1994b. Projectile compositions and modal frequencies on the "Chemistry of Micrometeoroids" LDEF experiment. In *LDEF—69 months in space,* vol. 2, edited by Levine A. S. Washington, D.C.: National Aeronautics and Space Administration. pp. 551–573.

Bradley J. P. 2003. The astromineralogy of interplanetary dust particles. In *Astromineralogy*, edited by Henning T. Berlin-Heidelberg: Springer Verlag. pp. 217–235.

Bradley J. P. 1994. Chemically anomalous, preaccretionally irradiated grains in interplanetary dust from comets. *Science* 265: 925.

Britt D. T. and Consolmagno G. J. 1996. The porosity of asteroids and meteorites: First results from the Vatican collection. *Bulletin of the American Astronomical* Society 28:1106.

Brownlee D. E., Joswiak D., Bradley J. P., and Hörz F. 1994. Interplanetary meteoroid debris in LDEF metal craters. In *LDEF—69 months in space,* vol. 2, edited by Levine A. S. Washington, D. C.: National Aeronautics and Space Administration. pp. 577–584.

Brownlee D. E., Tsou P., Anderson J. D., Hanner M. S., Newburn R. L., Sekanina Z., Clark B. C., Hörz F., Zolensky M. E., Kissel J., McDonnell J. A. M., Sandford S. A., and Tuzzolino A. J. 2003. Stardust: Comet and interstellar dust sample return mission. *Journal of Geophysical Research* 108, doi: 10.1029/2003JE002087.

Brownlee D., Tsou P., Aléon J., Alexander C. M. O'D., Araki T., Bajt S., Baratta G. A., Bastien R., Bland P., Bleuet P., Borg J., Bradley J. P., Brearley A., Brenker F., Brennan S., Bridges J. C., Browning N., Brucato J. R., Brucato H., Bullock E., Burchell M. J., Busemann H., Butterworth A., Chaussidon M., Cheuvront A., Chi M., Cintala M. J., Clark B. C., Clemett S. J., Cody G., Colangeli L., Cooper G., Cordier P. G., Daghlian C., Dai Z., D'Hendecourt L., Djouadi Z., Dominguez G., Duxbury T., Dworkin J. P., Ebel D., Economou T. E., Fairey S. A. J., Fallon S., Ferrini G., Ferroir T., Fleckenstein H., Floss C., Flynn G., Franchi I. A., Fries M., Gainsforth Z., Gallien J.-P., Genge M., Gilles M. K., Gillet P., Gilmour J., Glavin D. P., Gounelle M., Grady M. M., Graham G. A., Grant P. G., Green S. F., Grossemy F., Grossman L., Grossman J., Guan Y., Hagiya K., Harvey R., Heck P., Herzog G. F., Hoppe P., Hörz F., Huth J., Hutcheon I. D., Ishii H., Ito M., Jacob D., Jacobsen C., Jacobsen S., Joswiak D., Kearsley A. T., Keller L., Khodja H., Kilcoyne A. L. D., Kissel J., Krot A., Langenhorst F., Lanzirotti A., Le L., Leshin L., Leitner J., Lemelle L., Leroux H., Liu M.-C., Luening K., Lyon I., MacPherson G., Marcus M. A., Marhas K., Matrajt G., Meibom A., Mennella V., Messenger K., Mikouchi T., Mostefaoui S., Nakamura T., Nakano T., Newville M., Nittler L. R., Ohnishi I., Ohsumi K., Okudaira K., Papanastassiou D. A., Palma R., Palumbo M. O., Pepin R. E., Perkins D., Perronnet M., Pianetta P., Rao W., Rietmeijer F., Robert F., Rost D., Rotundi A., Ryan R., Sandford S. A., Schwandt C. S., See T. H., Schlutter D., Sheffield-Parker

J. A., Simionovici S., Sitnitsky S. I., Snead C. J., Spencer M. K., Stadermann F. J., Steele A., Stephan T., Stroud R., Susini J., Sutton S. R., Taheri M., Taylor S., Teslich N., Tomeoka K., Tomioka N., Toppani A., Trigo-Rodríguez J. M., Troadec D., Tsuchiyama A., Tuzolino A. J., Tyliszczak T., Uesugi K., Velbel M., Vellenga J., Vicenzi E., Vincze L., Warren J., Weber I., Weisberg M., Westphal A. J., Wirick S., Wooden D., Wopenka B., Wozniakiewicz P. A., Wright I., Yabuta H., Yano H., Young E. D., Zare R. N., Zega T., Ziegler K., Zimmerman L., Zinner E., and Zolensky M. 2006. Comet Wild 2 under a microscope. *Science* 314:1711–1716.

Burchell M. J., Cole M. J., McDonnell J. A. M., and Zarnecki J. C. 1999. Hypervelocity impact studies using the 2 MV Van de Graaff dust accelerator and two stage light-gas gun of the University of Kent at Canterbury. *Measurement Science and Technology* 10:41–50.

Burchell M. J. and Mackay N. G. 1998. Crater ellipticity in hypervelocity impacts on metals. *Journal of Geophysical Research* 103:22,761–22,774.

Burchell M. J., Foster N. J., Kearsley A. T., and Creighton J. A. Identification of mineral impactors in hypervelocity impact craters in aluminium by Raman spectroscopy of residues. *Meteoritics & Planetary Science* 43. This issue.

Chi M., Ishii H., Dai Z. R., Toppani A., Joswiak D. J., Leroux H., Zolensky M., Keller L. P., Browning N. D., and Bradley J. P. 2007. Does comet Wild 2 contain GEMS (abstract #2010)? 38th Lunar and Planetary Science Conference. CD-ROM.

Davoisne C., Djouadi Z., Leroux H., D'Hendecourt L., Jones A., and Deboffle D. 2006. The origin of GEMS in IDPs as deduced from microstructural evolution of amorphous silicates with annealing. *Astronomy and Astrophysics* 448:L1–L4.

Flynn G. J., Bleuet P., Borg J., Bradley J. P., Brenker F. E., Brennan S., Bridges J., Brownlee D. E., Bullock E. S., Burghammer M., Clark B. C., Dai Z. R., Daghlian C. P., Djouadi Z., Fakra S., Ferroir T., Floss C., Franchi I. A., Gainsforth Z., Gallien J.-P., Gillet P., Grant P. G., Graham G. A., Green S. F., Grossemy F., Heck P., Herzog G. F., Hoppe P., Hörz F., Huth J., Ignatyev K., Ishii H. A., Janssens K., Joswiak D., Kearsley A. T., Khodja H., Lanzirotti A., Le L., Leitner J., Lemelle L., Leroux H., Luening K., MacPherson G. J., Marhas K. K., Marcus M. A., Matrajt G., Nakamura T., Nakamura-Messenger K., Nakano T., Newville M., Papanastassiou D. A., Pianetta P., Rao W., Riekel C., Rietmeijer F. J. M., Rost D., Schwandt C. S., See T. H., Sheffield-Parker J., Simionovici A., Sitnitsky I., Snead C. J., Stadermann F. J., Stephan T., Stroud R. M., Susini J., Suzuki Y., Sutton S. R., Taylor S., Teslich N., Troadec D., Tsou P., Tsuchiyama A., Uesugi K., Vekemans B., Vicenzi E. P., Vincze L., Westphal A. J., Wozniakiewicz P., Zinner E., and Zolensky M. E. 2006. Elemental compositions of comet 81P/Wild 2 samples collected by Stardust. *Science* 314:1731–1735.

Gee D. J. 2003. Plate penetration by eroding rod projectiles. *International Journal of Impact Engineering* 28:377–390.

Graham G. A., Kearsley A. T., Wright I. P., Grady M. M., Drolshagen G., McBride N. M., Green S. F., Burchell M. J., Yano H., and Elliott R. 2001. Analysis of impact residues on spacecraft surfaces: Possibilities and problems. Proceedings, Third European Conference on Space Debris. pp. 197–203.

Graham G. A., Teslich N., Dai Z., Bradley J. P., Kearsley A. T., and Hörz F. P. 2006. Focused ion beam recovery of hypervelocity impact residue in experimental craters on metallic foils. *Meteoritics & Planetary Science* 41:159–165.

Greenberg J. M. and Gustafson B. Å. S. 1981. A comet fragment model for Zodiacal light particles. *Astronomy and Astrophysics* 93:35–42.

Hoppe P., Stadermann F. J., Stephan T., Floss C., Leitner J., Marhas K. K., and Hörz F. P. 2006. SIMS studies of Allende projectiles fired into Stardust-type aluminium foils at 6 km/s. *Meteoritics & Planetary Science* 41:197–209.

Hörz F., Fechtig H., and Janicke J. 1983. Morphology and chemistry of projectile residue in small experimental impact craters. Proceedings, 14th Lunar and Planetary Science Conference. pp. B353–B363.

Hörz F., Cintala M. J., Bernhard R. P., and See T. H. 1994. Dimensionally scaled penetration experiments: Aluminum targets and glass projectiles 50 μm to 3.2 mm in diameter. *International Journal of Impact Engineering* 15:257–280.

Hörz F., Cintala M. J., Zolensky M. E., Bernhard R. P., Davidson W. E., Haynes G., See T. H., Tsou P., and Brownlee D. E. 1998. Capture of hypervelocity particles with low-density aerogel. NASA/TM Technical Report 98-201792. 59 p.

Hörz F., Bastien R., Borg J., Bradley J. P., Bridges J. C., Brownlee D. E., Burchell M. J., Cintala M. J., Dai Z. R., Djouadi Z., Dominguez G., Economou T. E., Fairey S. A. J., Floss C., Franchi I. A., Graham G. A., Green S. F., Heck H., Hoppe P., Huth J., Ishii H., Kearsley A. T., Kissel J., Leitner J., Leroux H., Marhas M., Messenger K., Schwandt C. S., See T. H., Snead S., Stadermann F. J., Stephan T., Stroud R., Teslich N., Trigo-Rodríguez J. M., Tuzzolino A. J., Troadec D., Tsou P., Warren J., Westphal A., Wozniakiewicz P. J., Wright I., and Zinner E. 2006. Impact features on Stardust and comet Wild 2 dust. *Science* 314:1716–1719.

Kearsley A. T., Drolshagen G., McDonnell J. A. M., Mandeville J.-C., and Moussi A. 2005. Impacts on Hubble Space Telescope solar arrays: Discrimination between natural and man-made particles. *Advances in Space Research* 35:1254–1262.

Kearsley A. T., Burchell M. J., Hörz F., Cole M. J., and Schwandt C. S. 2006. Laboratory simulation of impacts upon aluminium foils of the Stardust spacecraft: Calibration of dust particle size from comet Wild 2. *Meteoritics & Planetary Science* 41: 167–180.

Kearsley A. T., Graham G. A., Burchell M. J., Cole M. J., Dai Z. R., Teslich N., Bradley J. P., Chater R., Wozniakiewicz P. A., Spratt J., and Jones G. 2007. Analytical scanning and transmission electron microscopy of laboratory impacts on Stardust aluminum foils: Interpreting impact crater morphology and the composition of impact residues. *Meteoritics & Planetary Science* 42:191–210.

Keller L. P. and Messenger S. 2006. The nature of the early solar system and presolar materials. *Journal of Mineralogical and Petrological Sciences* 101:122–129.

Leitner J., Stephan T., Kearsley A. T., Hörz F., Flynn G. J., and Sandford S. A. 2008. TOF-SIMS analysis of crater residues from Wild 2 cometary on Stardust aluminum foil. *Meteoritics & Planetary Science* 43. This issue.

Leroux H., Borg J., Troadec D., Djouadi Z., and Hörz F. P. 2006. Microstructural study of micron-sized craters simulating Stardust impacts in aluminium 1100 targets. *Meteoritics & Planetary Science* 41:181–196.

Leroux H., Stroud R., Dai. Z., Graham G., Troadec D., Bradley J., Teslich N., Borg J., Kearsley A., and Hörz F. 2007. Transmission electron microscopy of cometary residues from micron-sized craters in the Stardust Al foils. *Meteoritics & Planetary Science* 43. This issue.

Levine A. S., editor. 1993. *LDEF—69 months in space*. Washington, D.C.: National Aeronautics and Space Administration. 561 p.

Lodders K. 2001. Solar system abundances and condensation temperatures of the elements. *The Astrophysical Journal* 591: 1220–1247.

Love S. G., Brownlee D. E., King N. L., and Hörz F. 1995. Morphology of meteoroid and debris impact craters formed in soft metal targets on the LDEF satellite. *International Journal of Impact Engineering* 16:405–418.

McKeegan K. D., Aléon J., Bradley J., Brownlee D., Busemann H., Butterworth A., Chaussidon M., Fallon S., Floss C., Gilmour J., Gounelle M., Graham G., Guan Y., Heck P. R., Hoppe P., Hutcheon I. D., Huth J., Ishii H., Ito M., Jacobsen S. B., Kearsley A., Leshin L. A., Liu M.-C., Lyon I., Marhas K., Marty B., Matrajt G., Meibom A., Messenger S., Mostefaoui S., Nakamura-Messenger K., Nittler L., Palma R., Pepin R. O., Papanastassiou D. A., Robert F., Schlutter D., Snead C. J., Stadermann F. J., Stroud R., Tsou P., Westphal A., Young E. D., Ziegler K., Zimmermann L., and Zinner E. 2006. Isotopic compositions of cometary matter returned by Stardust. *Science* 314:1724–1728.

Messenger S., Keller L. P., Stadermann F. J., Walker R. M., and Zinner E. 2003. Samples of stars beyond the Solar System: Silicate grains in interplanetary dust. *Science* 300:105–108.

Rietmeijer F. J. M. 1998. Interplanetary dust particles. In *Planetary materials,* edited by Papike J. J.. Reviews in Mineralogy vol. 36. pp. 1–95.

Rutledge A. K., Roberts J. A., Orsi T. H., Bryant W. R., and Kotilainen A. T. 1995. Geotechnical properties and consolidation characteristics of North Pacific sediments, Sites 881, 883, and 885/886. In *Proceedings of the Ocean Drilling Program, Scientific Results*, edited by Rea D. K., Basov I. A., Scholl D. W., and Allan J. F. 145:525–546.

Schultz P. H. and Gault D. E. 1985. Clustered impacts—Experiments and implications. *Journal of Geophysical Research* 90:3701–3732.

Stadermann F. J., Floss C., and Bose M. 2007. Correlated high spatial resolution elemental and isotopic characterization of Wild 2 cometary samples (abstract #1334). 38th Lunar and Planetary Science Conference. CD-ROM.

Stadermann F. J., Hoppe P., Floss C., Heck P. R., Hörz F., Huth J., Kearsley A. T., Leitner J., Marhas K. K., McKeegan K. D., and Stephan T. 2007. Stardust in Stardust—The C, N, and O isotopic compositions of Wild 2 cometary matter in Al foil impacts. *Meteoritics & Planetary Science* 43. This issue.

Stöffler D. 1982. Density of minerals and rocks under shock compression. In Cermák V., Huckenholz H.-G., Rybach L., Schmid R., Schopper J. R., Schuch M., Stöffler D., and Wohlenberg J. *Numerical data and functional relationships in science and technology.* Group V Geophysics and Space Research, vol. 1, subvol. A. Berlin-Heidelberg: Springer. pp. 120–183.

Tsou P., Brownlee D. E., Sandford S. A., Hörz F., and Zolensky M. E. 2003. Wild 2 and interstellar sample collection and Earth return. *Journal of Geophysical Research* 108, doi:10.1029/2003JE002109.

Westphal A. J., Bastien R. K., Borg J., Bridges J., Brownlee D. E., Burchell M. J., Cheng A. F., Clark B. C., Djouadi Z., Floss C., Franchi I., Gainsforth Z., Graham G., Green S. F., Heck P. R., Hor'anyi M., Hoppe P., Hörz F., Joachim Huth J., Kearsley A., Leroux H., Marhas K., Nakamura-Messenger K., Sandford S. A., See T. H., Stadermann F., Tsitrin S., Tsou P., Warren J. L., Wozniakiewicz P. J., and Zolensky M. E. 2007. Discovery of non-random spatial distribution of impacts in the Stardust cometary collector. *Meteoritics & Planetary Science* 43. This issue.

Zolensky M. E., Zega T. J., Yano H., Wirick S., Westphal A. J., Weisberg M. K., Weber I., Warren J. L., Velbel M. A., Tsuchiyama A., Tsou P., Toppani A., Tomioka N., Tomeoka K., Teslich N., Taheri M., Susini J., Stroud R., Stephan T., Stadermann F. J., Snead C. J., Simon S. B., Simionovici A., See T. H., Robert F., Rietmeijer F. J. M., Rao W., Perronnet M. C., Papanastassiou D. A., Okudaira K., Ohsumi K., Ohnishi I., Nakamura-Messenger K., Nakamura T., Mostefaoui S., Mikouch T., Meibom A., Matrajt G., Marcus M. A., Leroux H., Lemelle L., Lanzirotti A., Langenhorst F., Krot A. N., Keller L. P., Kearsley A. T., Joswiak D., Jacob D., Ishii H., Harvey R., Hagiya K., Grossman L., Grossman J. N., Graham G. A., Gounelle M., Gillet Ph., Genge M. J., Flynn G., Ferroir T., Fallon S., Ebel D. S., Dai Z. R., Cordier P., Clark B., Chi M., Butterworth A. L., Brownlee D. E., Bridges J. C., Brennan S., Brearley A., Bradley J. P., Bleuet P., Bland P. A., and Bastien R. 2006. Mineralogy and petrology of comet Wild 2 nucleus samples. *Science* 314:1735–1739.